Ultrafast Studies of Dilute Magnetic Semiconductor Spin Excitations

by

Paul W. Jacobs

A dissertation submitted in partial fulfillment
of the requirements for the degree of
Doctor of Philosophy
(Electrical Engineering)
in The University of Michigan
2009

Doctoral Committee:
        Professor Roberto D. Merlin, Chair
        Professor Theodore B. Norris
        Professor Roseanne J. Sension
        Professor Duncan G. Steel

Do no evilness because it is a small one; do not leave a small

deed undone because it is just a petty one.

—Liu Bei

To Robin and Lisa

Acknowledgments

As every book, this work is based on the work of many others and with the support of many. At the University of Michigan, I owe much to Professor Roberto Merlin for his guidance and advice. Professor Duncan Steel provided a great deal of encouragement and support that allowed me to continue work on my PhD. My graduate student mentors, Jared Wahlstrand and Adrienne Stiff taught me a great deal about experimental physics. Outside of Michigan, our group has been fortunate to have samples given to us by Professors Bhattacharya and Uher at the University of Michigan, Professor Furdyna at Notre Dame, Dr. Florent Perez at INSP in Paris, and Dr. Pfeiffer and Dr. West at Lucent.

I have also been fortunate to have a great group of fellow students to work alongside. Much of the work here is based on earlier work by Jimin Bao, Andrea Bragas, and Daimian Wang. Jared Wahlstrand and Cynthia Aku-Leh worked alongside me on some of the experiments. Others that I have been able to work with include Mariano Trigo, Ilya Vugmeyster, Tobias Eckhause, Jingjing Li, Lei Jiang, and Andrea Bianchi.

Getting to this point has also required instruction and guidance from a number of teachers including Mr. Akenbrandt, Mrs. Paxton, Professor Valk, Professor O'Shea, and Dr. Welch. I have had the benefit of many great professors at Georgia Tech, Universitaet Stuttgart, and the University of Michigan.

Over the years, my friends and family have been very supportive; my Aunt Beth, Uncle Carl and their family, and Aunt Chris, Uncle Mike and Henry have provided places to work and refocus away from work. Matt, John, Tom and Betsy have frequently been a great distraction on occasion as well. My grandparents have provided continual support,

and Douglas and Betty Wallace a great source of inspiration. My parents have always been encouraging. My sister Robin has always been a great help in more ways than I can enumerate here, and my wife has always been a constant source of support.

Table of Contents

List of Figures

Abstract

Ultrafast measurement of dilute magnetic semiconductors has been intense over the last decade due to applications in spintronics. This thesis describes the use of optical measurements, both spontaneous scattering and impulsive stimulated scattering, to study two dilute magnetic semiconductors.

In the (Cd,Mn)Te system, two sets of experiments are presented here. In this system, Mn acts as a column 2 alloy, allowing the growth of high quality magnetic semiconductors. Using a spatial light modulator to create shaped pulses, we demonstrate coherent control of entangled bound electrons in this material system. First, we demonstrate the capabilities of such a system by coherently controlling the charge density modes in a GaAs quantum well. Then, the same technique is applied to a CdMnTe quantum well with electrons bound to unintentional donors. A pair of pulses is constructed to provide ideal destruction of the signal from a single bound electron spin flip, leaving the signal for the double spin flip. Additional data demonstrates the linear nature of the pump-probe signal of the single and double spin flip.

The second set of experiments presented here in (Cd,Mn)Te involve studying the decay of the collective spin flip wave in a 2DEG formed in a high quality CdMnTe quantum well. The collective spin wave mode is observed in pump-probe measurement data. Pump-probe measurements demonstrate the effects of spin polarization, heating, and carrier population on the lifetime of the spin wave. A decrease in spin polarization due to lower Mn concentration or lower magnetic field decreases the lifetime of the spin flip wave. The temperature of the sample is measured by fitting the frequency of the spin flip wave to the

Brillouin function. The spin wave lifetime rapidly decreases with small amounts of laser heating. Additionally, multiple temperature zones due to laser heating are observed with sufficient laser pump power. Carriers injected with the laser energy above the absorption edge decrease the lifetime.

The semiconductor system (Ga,Mn)As has been one of the most studied dilute magnetic semiconductors due to the advanced state of GaAs growth and fabrication technology. In this system, ferromagnetic behavior between the Mn atoms is mediated by hole carriers. As a substitutional alloy replacing Ga, Mn acts as an acceptor, creating the holes necessary for ferromagnetism. However, Mn is not an ideal acceptor, and at low temperatures holes become bound to the Mn acceptors. In heavily doped, ferromagnetic GaMnAs, paramagnetic regions persist containing holes bound to Mn acceptors. Previously, transitions between bound hole states were studied using inelastic scattering. In this work, the selection rules observed are determined to be the result of the relative spin populations of the Zeeman split spin states. A second set of pump-probe experiments performed on thin GaMnAs layers show that the highly interface-dependent magnon modes depend strongly on the As source used during growth.

Chapter 1

Introduction

1.1 Dilute magnetic semiconductors

Dilute magnetic semiconductors have attracted a great deal of interest due to their unusual properties. A small amount of a magnetic element, such as Fe or Mn, introduced into a semiconductor lattice during epitaxial growth greatly alters the behavior of carrier spins within the system. In the case of Mn and Fe, this is due to the 5 unpaired d electrons, which remain in the core of the atom while the outermost s electrons participate in bonds within the lattice. These systems are of great interest for spintronics, quantum information technologies, and optoelectronics (1).

The carriers in these systems act as an indirect exchange mechanism between non-neighboring magnetic dopants as defined by $H_{ex} = J^{sp-d} \mathbf{R}_i S_i \sigma$ with J^{sp-d} being the sp-d exchange coupling constant between the sp-like states of the band electrons and the d electron levels of the magnetic ions, $\mathbf{R}_i$ being the coordinate of the carrier with respect to the magnetic ion i, and S_i and σ being the spin operators of the magnetic ion i and the carrier (2). This can result in ferromagnetic behavior in heavily doped materials. A dopant such as Mn in GaAs will behave ferromagnetically due to the carrier interaction despite the anti-ferromagnetic behavior of MnAs. However, large Mn concentrations in GaAs and CdTe can result in the formation of Mn clusters that behave anti-ferromagnetically and do not contribute to ferromagnetic behavior.

In GaAs, Mn can act as a p-type dopant as well as a magnetic ion when it displaces a Ga atom. Because of the relatively low temperatures at which it must be grown, however, the quality of GaMnAs is generally poor. Additionally, the concentration of Mn in GaAs is limited to under 5-6% due to solubility limits (3). In comparison, II-VI semiconductors incorporate Mn as a column II metal replacing Cd, which results in an alloy, not doping, and more optimal growth conditions. Because of this, CdMnTe can be grown up to 77% Mn, at which point the crystal structure changes from zincblende to NiAs structure (2). Even higher concentrations can be grown epitaxially under strain. The end compounds, MnAs and MnTe are antiferromagnetic because of the Mn-Mn antiferromagnetic interaction.

In this work we perform optical measurements on a CdTe/MnTe superlattice, a very high quality modulation doped CdMnTe quantum well, and thin GaMnAs layers. In the first two cases, we are interested in the behavior of the carriers within the CdMnTe layers under applied magnetic fields. The Mn greatly enhances the effect of magnetic fields on the carriers. In the first case, this allows us to entangle bound electrons by means of an optically excited exciton. In the second case, we can excite collective spin excitations among a two degree electron gas. In GaMnAs we are interested in the collective behaviors of the Mn spins in low applied magnetic fields.

1.2   Optical measurements

A variety of optical measurements have studied many excitations in solid systems. Phonons, magnons, polaritons, and excitons can be generated and detected optically in semiconductor crystal systems by pump-probe measurements or photon scattering (4; 5; 6). These interactions are often mediated by carriers while other excitations involve the carriers themselves. A variety of mechanisms are responsible for these interactions such as laser heating and light-phonon interactions relying on light-electron interactions such as the Frölich interaction (7). Experimentally the optical properties of these materials and

excitations are sampled in many ways. In this work for instance, we measure the scattered light in spontaneous inelastic scattering spectroscopy or measure the intensity of a second laser pulse to sample the change in the sample's susceptibility, χ.

Spontaneous inelastic scattering (SIS) and impulsive stimulated inelastic scattering (ISIS) are sometimes fourier transforms of one another. Spontaneous scattering, or Raman scattering in the case of phonons, gives information directly in the frequency domain. The energy of the scattered light changes from that of the exciting light by the energy of the excitation created or destroyed. This scattered light is then spectrally resolved by a spectrometer. In impulsive scattering, a laser pulse shorter than the period of the excitation acts instantly relative to the scale of the excitation of interest. Ideally, it is sufficiently short to act as an instantaneous delta function force. The evolution over time of the optical properties of the sample is then measured by reflection of a second probing pulse.

Although complementary, the two measurements sometimes provide different information. This is especially true in resonance. Short laser pulses have broad spectrums that often coincide with multiple resonances, while continuous wave lasers can resolve each resonance individually. In other cases, such as measurement of long lifetimes or low frequency oscillations, the signal is much more easily accessible in impulsive stimulated inelastic scattering. On the other hand, impulsive stimulated inelastic scattering is limited in the frequencies it can observe due to the finite width of the exciting pulse, spontaneous inelastic scattering can measure much higher energy excitations. This limitation is being increasingly overcome as laser pulses become of sufficiently short duration that most excitations are within the pulse's bandwidth.

Furthermore, impulsive measurements allow the use of pulse shaping. Techniques have been developed for altering ultrafast optical pulses using acoustic waves in crystals and electronic control of liquid crystals (8). Optimal pulse shaping using genetic algorithms has been used to control chemical reactions and excitations. These pulse shapes can be used to enhance or destroy these excitations or promote or forbid chemical reactions. Additionally,

series of pulses can be tailored according to expected excitations periods constructively or destructively interfering with these excitations.

1.3 Summary

This work will be presented as follows. In chapter 2, details of the spontaneous inelastic scattering and pump-probe experimental apparatus are discussed. A variety of commercial laser systems are used as excitation sources, allowing us to resonantly excite samples across a broad range of photon energies. A magnetic cryostat maintained the temperature and external magnetic field while allowing optical access to the sample. The details of the pulse shaper set up for the experiments in chapter 3 are given. The procedures for generating the desired pulses are included. This setup is then used in an experiment to coherently control the collective modes in a GaAs quantum well, and data demonstrating such control is presented. Finally, the linear prediction algorithm used to analyze the data is discussed.

Experiments involving the entanglement of bound electrons are discussed in chapter 3. Electrons bound to donors in a CdMnTe quantum well were previously shown to be entangled by the optical excitation of excitons. It was proposed that, using a coherent control scheme, one could determine the spin state of the bound electrons. In this work, the pulse shaper is used to selectively excite spin states among the entangled donor bound electrons using specifically shaped pulses. Also, building on earlier measurements studying the resonant behavior at and slightly below the bandgap, spontaneous scattering is used to study the resonance behavior of the Mn spin flips above the bandgap, where free excitons are present, demonstrating a second resonance peak. Finally, measurements presented here of the spin flip excitation as a function of exciting power demonstrate the linear nature of the multiple spin flip signal.

Collective modes in a high mobility modulation doped CdMnTe quantum well are studied in chapter 4. The spin flip wave and single spin flip have been previously identified in

4

spontaneous inelastic scattering. In this work, the oscillations due to the spin flip wave are seen in pump-probe data. We analyze the various mechanisms responsible for the decay of this signal. The effects of spin polarization, laser heating, and optical generation of carriers are determined individually from the observed spin wave decay. The formation of previously predicted multiple temperature zones is also observed.

Experiments studying the role of defects in magnetic GaMnAs systems are covered in chapter 5. Magnon modes studied previously in thin layers of GaMnAs are used to determine the effects of the As species used during growth. The more reactive As_2 is known to create materials with lower defect concentrations, here it also forms better interfaces. In a second set of GaMnAs samples, the previously observed transition between bound Mn-related hole states in paramagnetic regions of otherwise ferromagnetic GaMnAs is studied further. The mechanism responsible for the inelastic scattering selection rules with regard to the incoming light polarization is determined.

Chapter 2

Experimental Techniques

2.1 Introduction

Ultrafast lasers have enabled us to study a variety of solid state excitations (4; 9; 10; 11). These lasers now have widths shorter than the oscillation periods of most spin and vibrational modes in solids and are tunable across the electronic resonances in common semiconductors. They are tunable from the UV using doubled and tripled Titanium-doped sapphire (called Ti-sapphire) lasers through the visible using OPAs to the IR using Ti-sapphire lasers. The tunable range of the ultrafast Ti-sapphire lasers used in our lab ranges from 730 nm to 820 nm, covering the bandgap range of most CdTe and GaAs based bulk and lower dimensional systems. The short widths available here, about 45 fs, enable us to generate excitations impulsively in a process we call impulsive stimulated inelastic scattering (ISIS). Phonons (12), polaritons (13), magnons (14), collective modes (15), and spin flips (16) are all impulsively excited with pulses of this duration. In this work, these ultrafast laser pulses are used to resonantly generate and detect spin flip excitations.

Complementing these ISIS measurements are spontaneous inelastic scattering (SIS) measurements. Using a variety of tunable continuous wave (CW) lasers and gas lasers, we can resonantly excite many of the same excitations as in the ultrafast measurements (17; 18; 19). The scattered light is measured by a Raman spectrometer providing a frequency-domain analog of our time-domain ISIS measurements.

First, I will discuss the laser systems used. Then I will describe the setup used for SIS. Next, I will describe our pump-probe setup including our pulse shaper and give an example of an earlier experiment demonstrating its use. After that the other equipment used in the lab will be discussed. Finally, I will detail the techniques used to analyze our time domain data.

2.2   Lasers

The basics of operation of all the lasers described here is covered in Siegman's Lasers book (20). All of our lasers used CW pump lasers to provide the population inversion necessary for lasing. For the dye laser and the CW Ti-sapphire laser, this was a Spectra-Physics 10 W Ar-ion laser. In the Ar CW laser, a tube of Ar gas is electrically excited with a high voltage. Energetic electrons ionize the Ar and then excite it to a higher level, which rapidly decays into lower energy levels. The Ar-ion laser has several narrow, discrete levels from which it can lase. When pumping other lasers, it is allowed to lase in all modes. The ultrafast Tsunami Ti-sapphire laser was pumped by a solid state Millenia V laser. This laser uses light provided via fibers from electrically pumped semiconductor diode lasers to pump a neodymium-doped yttrium vanadate crystal. The resulting 1064 nm light is then doubled to 532 nm by a lithium triborate crystal.

The CW Ti sapphire laser was pumped by the CW Ar-ion laser at 4 W. The laser is focussed onto the crystal with its polarization rotated to correspond to the Brewster angle to enter the crystal with minimal reflection. The Ar laser is absorbed by the Ti-sapphire crystal, which excites the crystal's electrons into a broad continuum of energy levels, which decay into lower energy levels in the band resulting in a population inversion (21; 22). The crystal lies at the focal point of two curved mirrors. The Ar light passes through these curved mirrors, but the luminescence from the Ti-sapphire is reflected. These mirrors serve to collimate the luminescence, which then reflects from the two mirrors that serve as the

ends of the cavity. The reflected light is then refocused onto the crystal by the curved mirrors. The population inversion in the crystal results in stimulated emission. One of the end mirrors is less than a perfect reflector and serves as the output coupler. In order to tune the wavelength at which the laser works, and to narrow the linewidth, a Lyot bi-refringent filter is placed in one of the arms of the laser cavity (23). The Ti-sapphire laser is able to lase over a large range of wavelengths (roughly 650 nm - 1100 nm) due to the continuum of levels it lases from. The Lyot filter selects on a series of wavelengths for which gain is allowed. When correctly designed, only one wavelength falls along the gain curve, resulting in a single, narrow laser line. Without the filter, the laser can produce about 500 mW of power, addition of the filter lowers it, depending on the wavelength, to no more than 300 mW of power.

The dye laser works under very similar premise and is also pumped by the Ar laser. We used a commercial Spectra-Physics model 375 dye laser. The cavity has all the same elements, two curved mirrors, the two end mirrors, and a bi-refringent filter similar to the one in the Ti-sapphire laser. Instead of a crystal, however, the dye laser has a stream of dye dissolved in a solvent. A pump recirculates the dye, and it is injected into the laser cavity through a nozzle. For the experiments in these studies the LDS 698 laser dye was used in a solvent mixture of ethylene glycol and propalene carbonate. It covers the wavelength range higher in energy than our CW Ti-sapphire laser (700-740 nm for our experiments) (24). Its power output was similar to the Ti-sapphire laser.

The Tsunami pulsed Ti-sapphire laser is a vertical cavity somewhat modified from the CW laser described above. Between the high reflection input mirror and the output coupler is the Ti-sapphire crystal as well as a pair of prisms with a slit between them. The position of the slit determines the wavelength while the rotation of the prisms determines the width of the pulse. The size of the slit can also be adjusted to optimize the laser for different pulse widths. With the mirrors used currently, the Ti-sapphire can be used with pulse durations of 45-300 fs and wavelengths between 725 and 820 nm without chirping. An acusto-optic

modulator (AOM) locks the laser repetition frequency to 82 MHz, and actively mode locks the system. The power is dependent on wavelength, but the maximum is roughly 650 mW of power around 800 nm. The system can be purged with nitrogen gas to remove water vapor absorption.

2.3 Spontaneous inelastic scattering

Our setup for SIS backscattering is depicted in Fig. 2.1. This setup allows us to use a narrow bandwidth, CW laser to excite a sample. The resulting light scattered from the excitation is collected and spectrally resolved. The practical details are as follows.

With Ar-ion lasers as the light source, a monochromator eliminates the lines resulting from luminescing plasma and a special high reflectivity mirror and prism combination is placed in the cavity to allow lasing at only a single wavelength. Combined, these eliminate the narrow extraneous plasma lines in the scattering data. A half wave plate is used to rotate the polarization of the laser to determine selection rules (7). A lens focuses the laser beam, which is directed onto the sample by a small mirror. The sample sits within a magnetic liquid He cryostat. The scattered light is collected by a lens that collimates the scattered light. The scattered light is then passed through a polarizer aligned along the more sensitive vertical polarization of the Dilor spectrometer and focused onto the entrance slit of the Dilor X-Y spectrometer by a fixed lens situated at the entrance. This lens is designed such that the scattered light is incident on the entire gratings, making optimal use of them. This is sometimes referred to as f# matching.

A pair of gratings and slits called the premonochromator on the Dilor blocks stray light, especially the elastically scattered laser allowing measurement of Raman spectrum relatively near the laser frequency. At 800 nm, we can approach to within about 5 cm^{-1} if the sample surface is of near perfect crystalline quality. The scattered light is then spectrally resolved by the spectrograph diffraction grating. A liquid nitrogen cooled CCD array col-
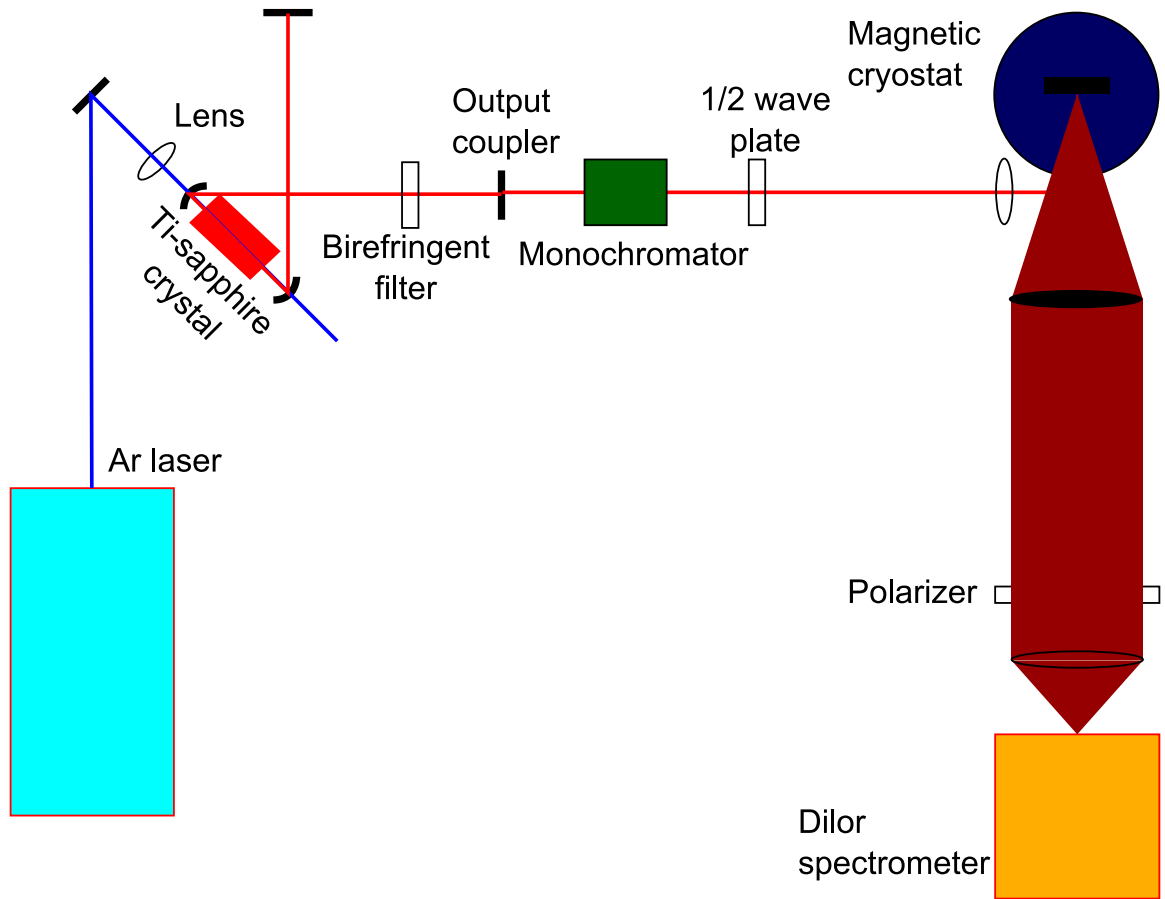
Figure 2.1 Stimulated inelastic scattering experimental setup

lects all of the spatially diverging spectrum simultaneously. Based on the voltage detected, and using a calibration, it estimates the number of photon counts.

Scattered light that has absorbed an excitation is called anti-Stokes scattering; it has higher energy than the incident laser. In the studies here, however, the scattered light is Stokes scattering with energy lower than the incident laser due to the creation of an excitation (7; 25). The energy of the Stokes peaks indicates the frequency of the excitation and the linewidth demonstrates the lifetime of the excitation. The premonochromator creates an edge in the scattering data, which appears peak-like in the data here at energies near the laser line, making the lowest energy Stokes line unreliable. Also in the spectrum appears the photoluminescence (PL) from the recombination of relaxed electron-hole pairs at the band edges, bound states, and excitons (26). Unlike SIS, however, the energy of the PL

does not shift in energy with the exciting laser line. It is therefore easily identifiable by taking data with 2 exciting wavelengths. Also sometimes appearing in the spectrum are plasma lines that were not entirely cut out by the monochromator (when the Ar laser is used) and occasional spikes due to collision of high energy cosmic rays with the detector.

Also mentioned in this work is photoluminescence excitation (PLE) data taken by other groups. In PLE, the spectrometer is set to the peak of a sample's luminescence. The exciting laser is tuned across the resonances of the sample. This results in a curve which, in some cases, is similar to the absorption of the sample (7). Although not always a perfect tool for measuring absorption, in high quality samples with few defects and no non-radiative decay mechanisms, the results should be similar. All of our samples fit within those parameters.

2.4   Impulsive stimulated inelastic scattering

The setup used for most of the ultrafast experiments here is shown in Fig. 2.2. These experiments focus on using ultrafast laser pulses to impulsively excite coherent excitations. Changes in the material's properties are probed by another laser pulse at a later time, which is measured by a photodetector. In the experimental setup, the pulsed laser beam from the Ti-sapphire laser is first sent through a pair of prisms. The pair of prisms acts as negative dispersion for the pulse, which counteracts the second order dispersion caused by other materials through which the pulses pass (27). Dispersion would otherwise stretch the pulses because the red and blue parts of the pulse spectrum travel at different speeds through dispersive media; the acusto-optical modulator (AOM) crystals particularly cause a high degree of dispersion. Higher orders of dispersion cannot be corrected in this manner, although it is possible to do so using a pulse shaper. For pulses of 45 fs and longer it is generally unnecessary to deal with higher orders of dispersion as their contribution is small compared to the width of the pulse. The spin oscillations of interest in our experiments had frequencies of less than 1 THz, and our setup easily operated in the impulsive limit with
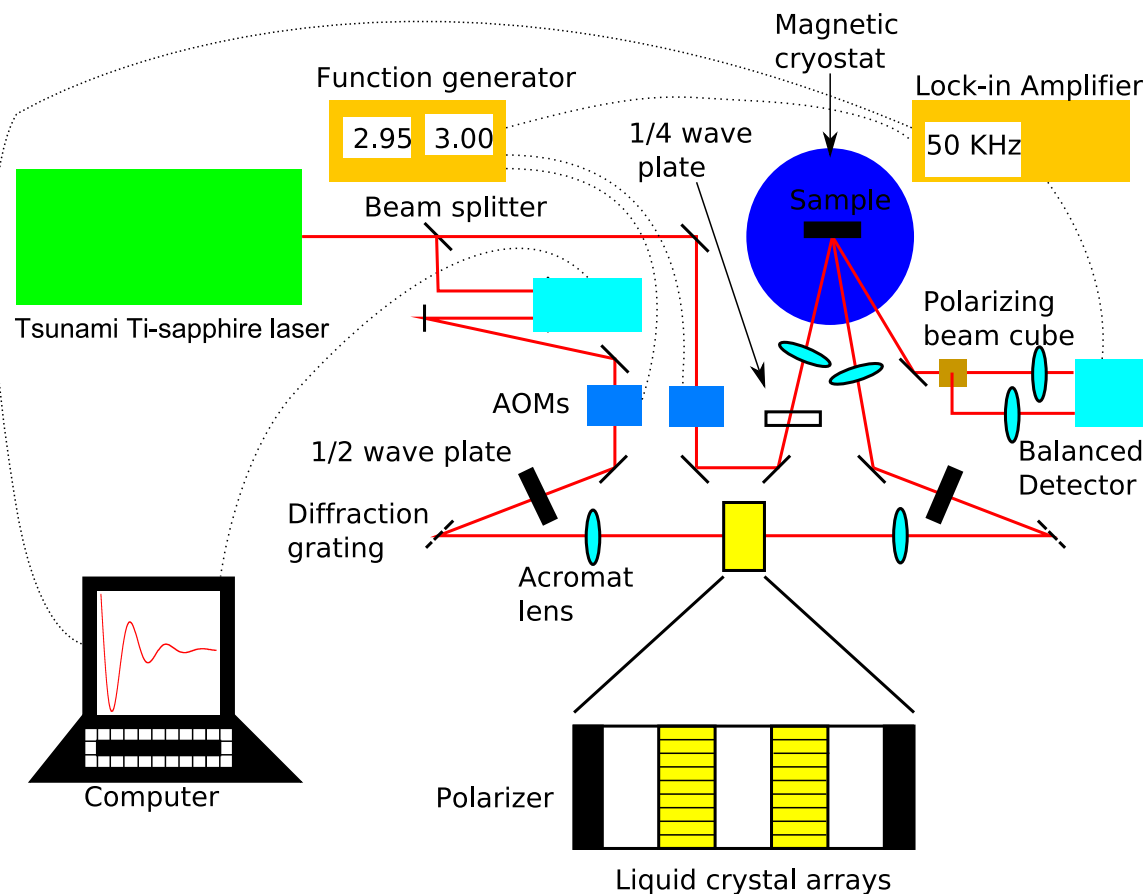
Figure 2.2 Pump probe experimental setup with polarization rotation measurement

pulses of less than 100 fs.

After the prisms, the beam is split with the majority of it, the pump, sent to a retrore-flector mounted on the translation stage to provide the temporal displacement of the pulse. This delay is controlled by a computer. The weaker portion of the pulse is the probe. Both pulses pass through separate AOMs. These are Tellurium Oxide crystals with transducers attached to them. The transducers produce a standing vibrational wave in the crystal that acts as a diffraction grating for the pulse, sending the first order beam off at an angle rela-tive to the the zeroth order. The standing waves are then modulated at different frequencies for the two beams up to a maximum of 3 MHz. This turns the first order on and off, acting as a chopper when an aperture is placed allowing only the first order beam through. The optimal modulation frequency has been determined using a spectrum analyzer with the de-

tector. Measuring the noise spectrum, we select a frequency with minimal noise (28). The most common noise is 1/f flicker noise, but there are many additional spikes from other sources in the lab.

After the AOMs, the pump beam is either sent through the pulse shaper setup detailed later in this chapter, or it is sent directly to the lenses before the sample. Wave plates create circularly polarized pump pulses or rotate the linear polarization. The probe is delayed to match the pump path length. Both beams are focused onto the sample to a spot size of approximately 100 microns. As the magnetic excitations are very sensitive to laser heating, the spot size sometimes is defocussed to lower the fluence.

The pump impulsively excites the sample, which can create a variety of coherent excitations (10). The well-developed formalism for phonons can be adapted for magnetic excitations (25). These excitations alter the susceptibility of the sample, which alters the intensity and polarization of the probe pulse (9). Earlier works have explored this process in detail (28; 29; 30). To measure the polarization rotation of the pump, after reflection, the probe is rotated 45 degrees using a half wave plate and split into perpendicular polarizations by a polarizing beam cube. Alternately, to measure reflectivity of the probe, a beamsplitter is used to pick off a reference beam, which is used to balance the reflected probe. In both cases, the two beams are detected by silicon photodiodes, and the signal subtracted and amplified within the Nirvana detector. The balanced detection setup eliminates noise from the laser common to both the probe and pump. The signal is sent into a Stanford Research Systems lock-in amplifier, which is connected to the two function generators that supply the signals to the AOMs and is locked in at the difference frequency. The basics of lock-in detection are discussed in the Art of Electronics (31) and the difference frequency mechanism is discussed in (29). This eliminates the signal from the pump light scattered off of the sample's surface, which creates a background signal if the pump beam only is chopped. A computer is used to collect the data from the lock-in amplifier.

A spectrometer is used to measure the spectral shape of the pulse, and a cross-

corollation measurement using the pump and probe determines the temporal extent of the pulses. If the result of the two measurements differ in resulting pulse width (directly measured in cross-corollation, and measured from a FFT of the spectrum), then it indicates that the pulse's width is partially a result of chirp. While this determines if and how much the pulse is chirped, it does not give the order. For further information, a frequency resolved optical grating (FROG) technique as described in the next section is useful. A β-Barium Borate (BBO) crystal doubles the light from the pump and probe beam for the cross-corollation measurements and detected using a photomultiplier (PMT) (32). The doubled signal from the pump and probe beams is optimized under phase matching conditions by rotating the crystal orientation. This technique is also used to calibrate the translation stage location, identifying the location at which the pump and probe pulses have zero delay.

2.5 Pulse shaping

The pulse shaper was based on a 256 pixel spatial light modulator from CRI. The setup is related in a paper by Wefers and Nelson (8). A grating is used to spatially disperse the pulse's spectrum, as shown in Fig. 2.3a. A lens collimates the diverging spectral elements while focusing them in the perpendicular direction onto the mask as shown in Fig. 2.3b. The mask is a set of two liquid crystal arrays of pixels that can be individually altered by applying a voltage across them. This allows the axis of the liquid crystals to shift, thus altering the polarization and phase of the light passing through the mask. A polarizer after the liquid crystals changes the polarization rotation into an amplitude change. The now masked spatial elements of the pulse are then refocused by a second lens onto a second grating that reforms it into a beam containing the desired pulse shape.

A Matlab script detailed in appendix A calculates the required voltages across the elements of the liquid crystal array. First, the retardance of a given pixel element is calibrated by measuring the power passing through at a series of voltages. The voltages are then
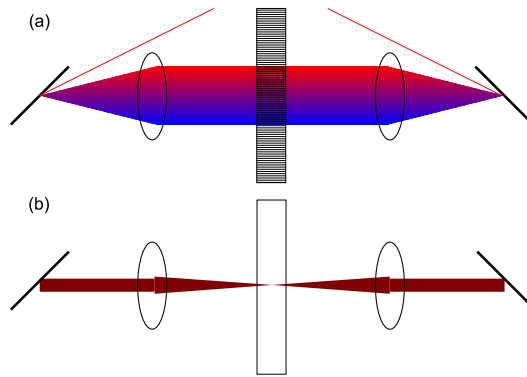
Figure 2.3 Layout of the spatial light modulator showing it from (a) above and (b) from the side.

extrapolated to allow any retardance needed. The spatial distribution of the pulse was measured experimentally by turning on selected pixels and using the spectrometer to determine the spectrum passed by that element. The Matlab script then calculates a complex transfer value for each of the pixels. This complex transfer value is then translated into an optical retardance for the two arrays and finally a calibration is used to determine the voltages to be applied to each liquid crystal element of the array.

Alignment of the pulse shaper is very important to prevent inadvertent alterations of the pulse. The pulse shaper is set up for a specific pulse width, in our case 100 fs, although it continues to work well for small deviations. To confirm the accuracy of the alignment, a FROG setup determined the resulting pulse shape (33; 34). The gratings were placed on translation stages, and an autocorrolator was used to monitor the pulse shape. The system is very sensitive to the distance between the gratings and the lenses. Any deviation from the focal point results in second order chirp, which expands the pulse and is easily measured by the FROG or the autocorrolator. Fig. 2.4 shows the results of a cross-corollation measurement demonstrating pulse shaping. In the middle of the two pulses is a much smaller figure that is the leakage of the original pulse around the elements of the LCD mask. Also, note that the two pulses are weaker due to loss from amplitude pulse shaping and the zeroth order of the gratings.
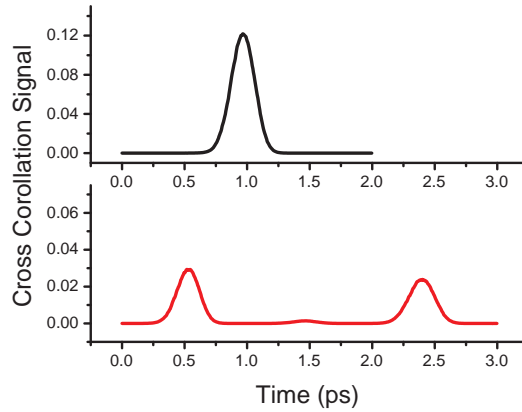
Figure 2.4 Cross-corollation measurements showing the original unmasked pulse and one with a mask creating two pulses.

2.5.1 Coherent control of charge density modes

Pulse shaping has demonstrated coherent control of phonons in semiconductor quantum wells (35), bulk semiconductors (36), and molecules (37). We have previously studied collective modes in a 2D electron gas in a high mobility modulation doped GaAs quantum well (38). The previously mentioned pulse shaping setup creates a pair of pulses separated by variable duration.

Our samples were GaAs quantum wells between AlGaAs barriers with modulation doping to create a high mobility two dimensional electron gas (2DEG). Optical pulses create several excitations within this 2DEG, dependent on the light's polarization (15). The excitations observed in our quantum well are the cyclotron resonance, the single particle excitation, the charge and spin density modes and coupled modes involving multiple excitations. The cyclotron resonance results from the collective oscillation of the 2DEG electrons in the plane of the quantum well around an externally applied magnetic field (39). While normally not observable in backscattering SIS, when coupled with other excitations in a tilted magnetic field that do interact with light perpendicularly incident, it becomes allowed (40). The single particle excitation involves oscillations of individual electrons between the energy sublevels of the quantum well, and is highly dependent on

16

the laser being in resonance (41). Two more collective modes appear for low k-vectors, the charge density excitation (CDE) and the spin density excitation (SDE) (42). Both involve the 2DEG electrons oscillating collectively perpendicular to the plane of the well in the lowest energy states of the well. In the spin density mode, the two electron spins oscillate out of phase, resulting in a lower energy, while for the charge density they oscillate together, resulting in higher energy due to Coulomb repulsion. In a tilted magnetic field, the CDE excitation couples to the cyclotron mode resulting in hybrid modes that diplay avoided crossings (43). Additionally, with sufficient laser pumping in resonance with the excited state of the quantum well, electrons are generated in the lowest excited level of the quantum well. The charge density modes involving the lowest two excited energy levels then become observable in SIS and pump-probe.

A summary of the SIS peak frequencies is shown in Fig. 2.5. The lines show the coupled cyclotron-charge density modes with their avoided crossing. Combined modes involving charge density plus and minus a cyclotron modes have also been identified and also show avoided crossings. The 1 THz signal appearing at higher magnetic fields was not identified. For these SIS measurements, the exciting power was low, and the excited state CDE was not observed. The time domain signals of the cyclotron, CDE, and SDE are shown in Fig. 2.6. At low magnetic field, this signal is dominated by the charge and spin density modes while at high magnetic field, the coupled CDE-cyclotron modes dominate the signal. The slow oscillation seen in the high magnetic field data is the lower branch of the coupled mode.

We then attempted to coherently control these collective excitations seen in a high magnetic field using a pair of pulses. The effect of the time separation between pump pulses on the amplitude of the collective modes is shown in Fig. 2.7 from (38). The amplitude of the CDE is expected to show a sinusoidal time dependence on the separation between pump pulses. The ground state CDE demonstrates this sinusoidal dependence with a period equal to that of the mode itself. The excited state mode demonstrates the general qualitative
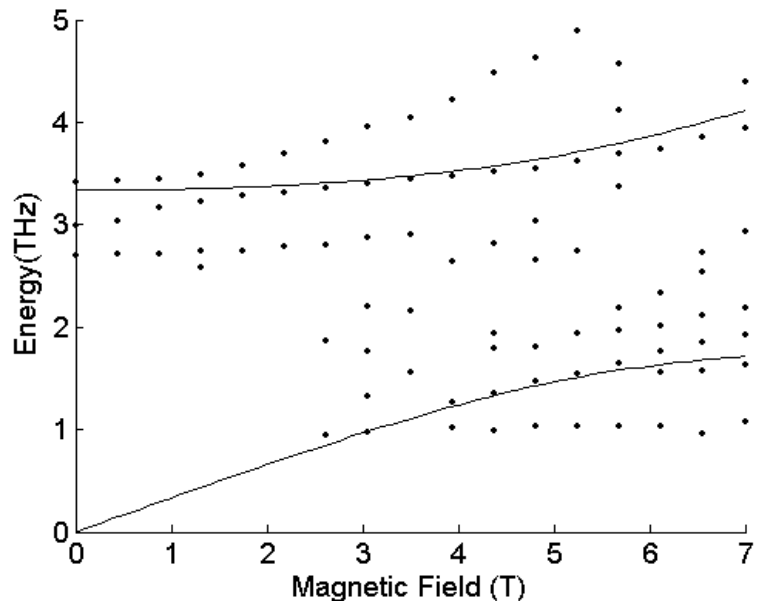
17

Figure 2.5 Summary of SIS data showing peak frequencies. The curves represent the local density approximation calculated frequencies for the coupled charge density-cyclotron modes
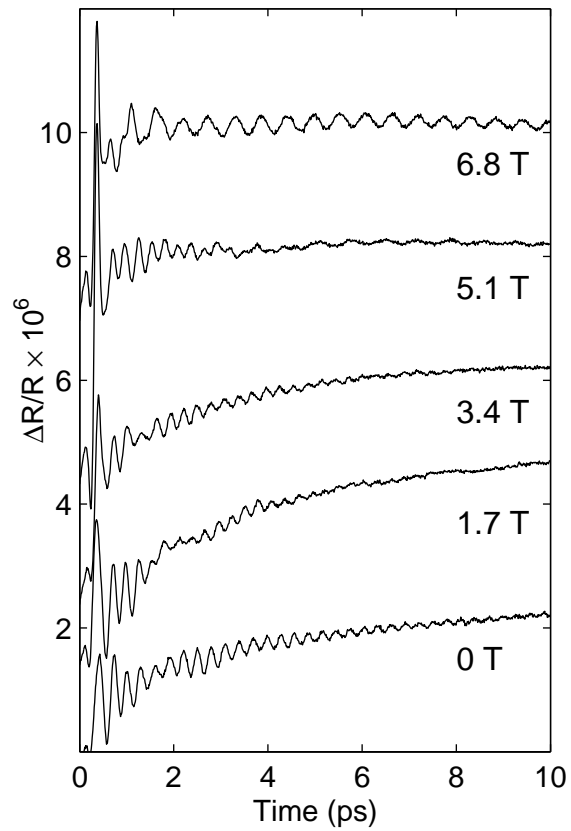

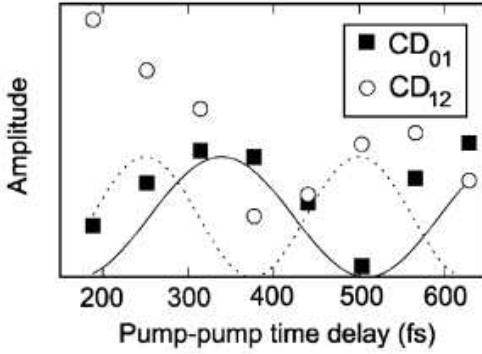**Figure 2.6** Time domain pump-probe data showing the cyclotron, CDE, and SDE excitations at several magnetic fields.

18

Figure 2.7 Coherent control of two charge density modes in a high mobility GaAs quantum well. CD_{01} refers to charge density oscillations involving the lowest two energy levels of the well and CD_{12} refers to oscillations involving the first and second excited states of the well.

oscillatory behavior at the right frequency, but is not sinusoidal. The deviation is likely the result of the coupling between the two collective modes that both involve the lowest excited state of the quantum well.

2.6   Other equipment

The cryostat used for all measurements was a Janis Optimag, model 12CNDT. It can provide magnetic fields up to 7 Tesla and the sample can be moved vertically and rotated to alter the direction of the magnetic field relative to the sample. It has 4 windows allowing backscattering, scattering at 45 degrees, and transmission measurements. Two heaters, one fixed to the He inlet and one fixed to the sample holder and two thermisters, one in the chamber below the sample and another on the sample holder allow control of the sample's temperature. This setup allows temperatures from 1.8 K for He immersion to room temperature. A controlled power supply is used to charge the magnet and then disconnected to provide a stable field.

Three detectors were used in ultrafast experiments. In most pump-probe measurements, the balanced detector was used a Nirvana (Model 2007). It is able to auto-balance to remove low frequency signals (and the DC level) below a specified frequency. Also used for some measurements was a balanced Si photodetector built by Jimin Bao with adjustable

sensitivity. To detect doubled light at 400 nm in cross-corrolation and autocorrolation measurements a Hamamatsu photomultiplier with adjustable gain was used.

2.7   Linear prediction

A linear prediction algorithm fits the data with a series of decaying exponentials and sinusoids (44). This procedure consists of describing a given point in the data as a linear function of the previous data points. A matrix is set up from the original data (with the time zero artifact removed), and is then diagonalized to produce the singular values. Because our data often has signals near the noise level, it is necessary to select where to truncate the singular values used by hand to get the best fit for the data. In the ideal, noiseless case, these singular values would be zero, but when noise is present, they take positive values. The selected singular values are then used to set up a polynomial, the roots of which yield complex values. From these complex values, we can calculate the frequency and decay constant of each of the decaying exponentials and sinusoids. A second least squares procedure then produces the corresponding amplitude and phase of the signal. Using these fit parameters, a spectrum of Lorentzian peaks can be constructed analogous to a FFT, but without noise.

Chapter 3

Coherent Control of Spin Flips in a CdMnTe quantum well

3.1 Introduction

Quantum information systems have the potential to dramatically speed many processes, including the factoring of large numbers, search algorithms, cryptography, and the simulation of other quantum systems (45; 46). By accelerating processes orders of magnitude, previously impossible problems become solvable. Traditional digital computers have a limited ability to simulate a quantum system for instance, and doing so for a system of any great complexity is difficult. DiVincenzo introduced a set of five standards needed to implement a functional quantum computer to perform these calculations (47). A variety of implementations possibly meeting these criteria include ion traps (48), NMR (49), and solid state systems (50; 51).

A key element of these systems needed for calculations is the ability to entangle quantum states. An entangled quantum state is not factorizable into independent expressions for the states of the particles (quantum bits) in the system (52). For a system of two quantum bits a and b, $|\psi\rangle = |0\rangle_a |0\rangle_b + |0\rangle_a |1\rangle_b + |1\rangle_a |0\rangle_b + |1\rangle_a |1\rangle_b$ can be factored into $|\psi\rangle = (|0\rangle_a + |1\rangle_a)(|0\rangle_b + |1\rangle_b)$. On the contrary, however, a system in the state $|\psi\rangle = |0\rangle_a |0\rangle_b + |1\rangle_a |1\rangle_b$ cannot be factored into expressions involving only a or only

b. The result is a state where bit *a* has a direct correspondence to the state of bit *b*. The example entangled state expressed here is the maximally entangled state for a system of two quantum bits.

Jimin Bao introduced a system of entanglement of electron spins within a dilute magnetic quantum well (53). His system met many of the criteria proposed by DiVincenzo. A known starting state is provided by the equilibrium alignment of the electron spins along a magnetic field in the plane of the quantum well at low temperature. Aligning with the field is energetically favorable due to the presence of Mn within the well and the spin coupling between the Mn and the electrons. At very low temperatures, any electron within the well will therefore be aligned in a well defined state. Next, the system needs a means of entangling the electrons within the well. Optical excitation of a heavy hole exciton introduces a perturbation to the magnetic field experienced by the electrons within the well. Due to spin-orbit coupling, the spin of the heavy hole is perpendicular to the externally applied magnetic field. This perturbation allows normally forbidden transitions between electron spin states. All electrons within the radius of the heavy hole experience the perturbation and may be entangled by it. DiVincenzo's next requires that the states be orthogonal. By conservation of spin, electrons within the quantum well cannot flip state without the intervention of an outside force. The states of the system also need to be long lived; This has not yet been addressed. The signal is broadened by the inhomogeneity of the electrons within the well. Due to random distribution of the Mn, the optically excited excitons, and the donors to which the electrons are bound, the forces applied to the spins vary widely. Variations in the quantum well's interface at the antiferromagnetic MnAs barriers may also decrease the lifetime. Finally, the final spin state of the electrons must be read. This is provided by optical means as well. A probe pulse optically samples the susceptibility of the well, with a resulting rotation of the polarization of the pulse. This rotation can then be measured with a balanced detector as described in chapter 2.

In this chapter, we will describe our technique for coherently controlling the spins of

the system using two pulses. Then the linear nature of the two electron spin flip excitation is demonstrated. Next we will present experimental data of such coherent control. Finally, we show SIS studies demonstrating the resonances of the well.

3.2 Material System

Our material system is a series of one hundred undoped 58 Å CdTe (bandgap at 2 K is 1.606 eV) quantum wells sandwiched between 19 Å MnTe (bandgap at 2 K is 3.2 eV) barriers grown by MBE (2). The MnTe layers are antiferromagnetic and the barrier height is such that carriers in the CdTe layers are strongly confined. While MnTe normally does not crystallize in the zincblende lattice structure, it is sufficiently thin here to grow as a highly strained zincblende material. The multiple quantum wells were grown on top of thick buffer layers of ZnTe and CdTe on a GaAs substrate. These thick layers reduce the strain and the number of defects in the subsequent layers.

During the course of epitaxial growth, the Mn from the barriers diffuses into the CdTe layers of the superlattice, resulting in layers of $Cd_{0.996}Mn_{0.004}Te$ in our sample (16). Also during growth, unintentional impurities from the growth chamber are incorporated into the lattice. The most common impurities are generally dopants, in the case of this sample this is likely In. Under certain growth conditions, In replaces Cd and acts as an electron donor (54). Earlier measurements estimated the In content participating as donors in the CdTe layers to be $5 \times 10^{16} cm^{-3}$ (16). At low temperatures, the donor's electrons are bound to the charged donor by Coulomb attraction.

3.3 Theory

The experimental setups used are described in chapter 2. For the experiments here, the external magnetic field in the Janis magnetic cryostat is applied in the plane of the quantum well. The five unpaired Mn d electrons responsible for magnetism align with the externally

applied field. These electron states lie far below the valence band, and are not directly involved in electronic transitions. However, through the exchange interaction given by $J^{sp-d}(r - R_i)S_i \cdot \sigma$, the electrons' spins align the nearby donor bound electrons along the field direction. The quantity J^{sp-d} represents the exchange coupling constant between the band electrons and the Mn d electrons, r and R_i represent the electron and Mn ion positions, and S_i and σ are the Mn electron and bound electron spin operators. The spin states are quantized along the external field axis.

The energy of these spin states are determined by the relation (2),

$$E = g_{eff}\mu_B H \tag{3.1}$$

with the effective electron g factor

$$g_{eff} = g - N_0\alpha x \langle S_z \rangle / \mu_B H \tag{3.2}$$

and for CdMnTe, $N_0\alpha = 0.22$ eV (55). The Mn concentration is x, H is the applied magnetic field, and g is the basic CdTe g factor. The average spin of the Mn d electrons, $\langle S_z \rangle$, for a spin 5/2 system is

$$\langle S_z \rangle = \frac{-5}{2}B_{5/2}(\mu_B g B / k_B T) \tag{3.3}$$

with $B_{5/2}$ the Brillouin function and T is the spin's temperature. With these equations, we can calculate the energy of the electron spin states of the system.

A laser in resonance with the exciton energy creates heavy hole-electron pairs. The heavy hole has a p-type orbital in the valence band with non-zero angular momentum. Because the heavy hole is confined by the quantum well's MnTe barriers, this angular momentum must be in the plane of the quantum well. Due to spin-orbit coupling, the spin of the heavy hole is therefore confined in a perpendicular direction, which in this case is the growth direction out of the plane of the quantum well (56; 57; 58; 59). This heavy hole spin introduces a new, temporary, localized magnetic field perpendicular to the externally
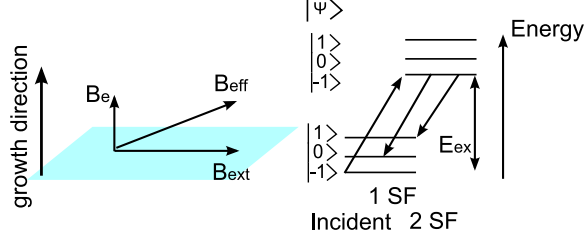
24

Figure 3.1 Depiction of the magnetic fields present in the CdMnTe layers and the transitions between spin states.

applied field, the Mn electron spins in the well, and the donor bound electrons. The magnetic field perturbation at the exciton is given by $B_{hh} = \kappa J/g\mu_B$, where κ is the coupling constant between the exciton and bound electron and J is the spin of the heavy hole. The external, exciton, and effective fields are depicted graphically in Fig. 3.1. While the heavy hole spin, at low fields, is along the growth direction as discussed here, at higher fields, the heavy hole begins to overcome the spin confinement of the well, and it becomes energetically favorable for the spin to rotate toward the external field (57). This is demonstrated with the approach of the spin flip frequency to a maximum at high magnetic fields /citeBao.

The exciton affects the local Mn as well, causing them to rotate about the new, local field. The exciton-Mn complex is referred to as a magnetic polaron (60), or if the exciton is bound, a bound magnetic polaron (61; 62). These excitations also show up in the pump-probe and SIS data, but are unrelated to the entanglement scheme.

For the entanglement scheme, the perturbation of the magnetic quantization axis by the presence of an exciton is critical. The Hamiltonian of the spin system can be written as, $H_0 = |a\rangle g_{eff}\mu_B S \cdot B \langle a|$. The bound electron spins (at low temperature), can not flip without a perturbation. With the new quantization axis created by the net magnetic field of the exciton and external field combined, we can project the old states onto the new axis. The perturbation is of the form of the electric dipole operator, which can be written $V = F |a\rangle d_{ab} \langle b|$ where F is the result of the $E \cdot d$ product. The total Hamiltonian of the

system under illumination is,

$$H = H_0 + V + H_{exciton} = |a\rangle g_{eff}\mu_B S \cdot B \langle a| + F |a\rangle d_{ab} \langle b| + |b\rangle g_{eff}\mu_B(-\kappa J/g_{eff}\mu_B) \langle b|$$

$$(3.4)$$

The number of electrons have their spins altered by a single exciton depends on the local lattice composition, the exciton radius, and the nature of κ. The exciton radius in bulk CdTe is 50 Å(16). The concentration of donor impurities can therefore be estimated from the multiple spin flip data. As a secondary effect, the degree of entanglement also depends upon how much the spin of the electrons has been rotated. This depends on the relative magnetic fields applied externally and on the exciton's heavy holes. Generally, this is a small value as the coupling allowed by the heavy hole's presence is small compared to the external field.

We have defined the state created by the pump pulse, so now we can study the effect on the probe pulse. Assuming the interaction between energy states is given by the dipole transition matrix element $\langle n|d|m\rangle$, we can define the optical response of the media as, (16)

$$\chi = \sum_l \frac{\langle \Psi|d|l\rangle \langle l|d|\Psi\rangle}{\hbar(\omega - \omega_l)} \tag{3.5}$$

with the effect on an incident laser pulse given by the index of refraction, $n = \sqrt{1+4\pi\chi}$ through the reflectivity, $r = (n-1)/(n+1)$ for a normally incident probe. Given the relatively large index of refraction of our materials, our reflected laser pulses are reasonably close to normal incidence.

3.4 Impulsive stimulated inelastic scattering

The time resolved signal of a single pulse is shown in Fig. 3.2. This pump-probe data was taken with an external magnetic field of 5.25 T at a temperature of 4K. The pulse width was 100 fs and centered at an energy of 1.71 eV, in resonance with the free excitons above
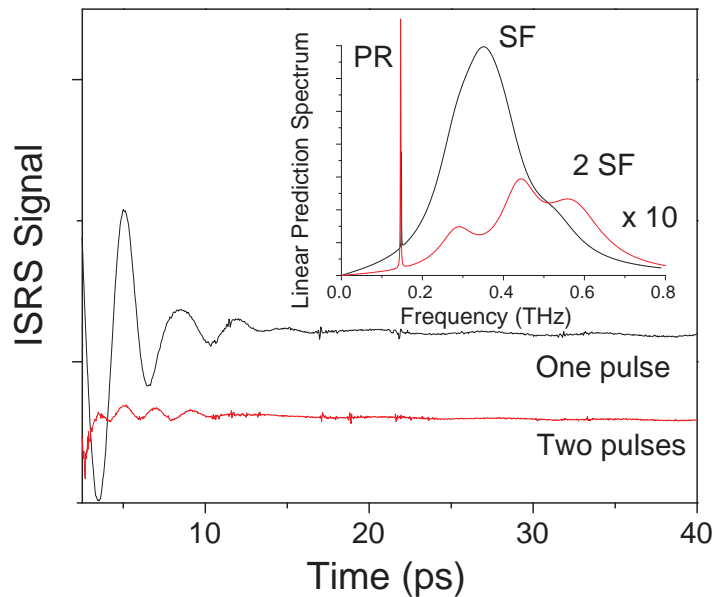
Figure 3.2 Time resolved signal from a single and two pulses separated by half the spin flip period. The inset contains the spectrums resulting from linear prediction fits to the data. SF is the signal of a single spin flip, 2 SF is the signal from 2 spin flips, and PR is the Mn spin flip.

the absorption edge. The pump was approximately 100 μm wide with a power of 4 mW and the probe was 3 mW with a slightly smaller diameter. The probe was linearly polarized, and the polarization rotation was detected as described in chapter 2. The pump was circularly polarized to selectively excite a single heavy hole spin direction.

The inset shows the spectrum of the linear prediction fit. The feature labeled PR in the inset indicates the long lived flip of a single Mn d electron spin called the paramagnetic resonance. The central peak, labeled SF is the spin flip of the single bound electron, and the 2 SF peak is the flip of two bound electrons simultaneously. The SF and 2 SF transition are depicted in Fig. 3.1. These signals decay within a few cycles, most likely due to inhomogenous broadening. The Mn are randomly distributed within the CdMnTe layers and the environment around the bound electrons can vary extensively. The additional peak between the SF and 2 SF peak indicates the flip of a bound electron spin in an excited state.

The signal in ISIS measurements shows different behavior from the earlier SIS data

27

(16; 60). An example of resonant SIS data taken on our sample is shown in Fig. 3.3. Six Mn d electron spin flips are visible in this data. Instead of multiple harmonics of the Mn d electron paramagnetic resonance, in ISIS only the single Mn spin flip signal is observed as the long lived signal at 140 GHz. However, we do observe the harmonics of the spin flip of electrons bound to donors. Only a single bound electron spin flip has been observed in the SIS data (63).

Next, ISIS measurements demonstrate that the harmonics of the spin flip observed in the ISIS measurements are a linear signal indicating the involvement of multiple donor bound electrons and not an optical overtone caused by a higher order term. This is important in our entanglement scheme, because a non-linear dependence on power would indicate interaction of light with non-interacting spins. Because the strength of the spin harmonics is orders of magnitude smaller than the single spin flip, the signal could be interpreted as optical harmonics. A linear dependence of the spin flip on pump power indicates that the light is interacting with a pair of spins connected through a common exchange mechanism. To demonstrate this linearity, we maintained a constant probe power, and adjusted the power of the pump between 3 and 11 mW. The beam size was ~100 microns across. Shown in Fig. 3.4 are the linear prediction amplitude fits of the SF and 2 SF from our experimental data. The offsets at zero pump power are due to a constant offset on the power detector.

Having now identified the spin state excitations and demonstrated their linearity, the next step is to coherently control the spin state of the system using multiple laser pulses. If we define a region of the sample with two bound electrons as $\Psi = C_{-1} |-1\rangle$ then the resulting state after a laser pulse can be written as $\Psi = C_{-1} e^{-iE_{-1}t/\hbar} |-1\rangle + C_0 e^{-iE_0 t/\hbar} |0\rangle + C_1 e^{-iE_1 t/\hbar} |0\rangle + ex.$ where $ex.$ represents the same states with an exciton present. Assuming that C_0 and C_1 are small compared with C_{-1} (that is, the perturbation is relatively small),
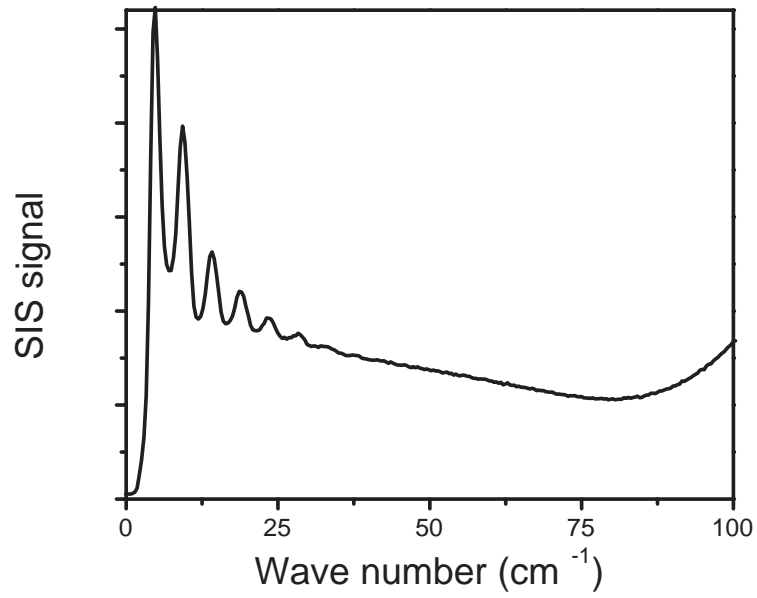
Figure 3.3 SIS data from the CdMnTe/MnTe sample at B = 2T with an exciting laser energy of 730.6 nm.
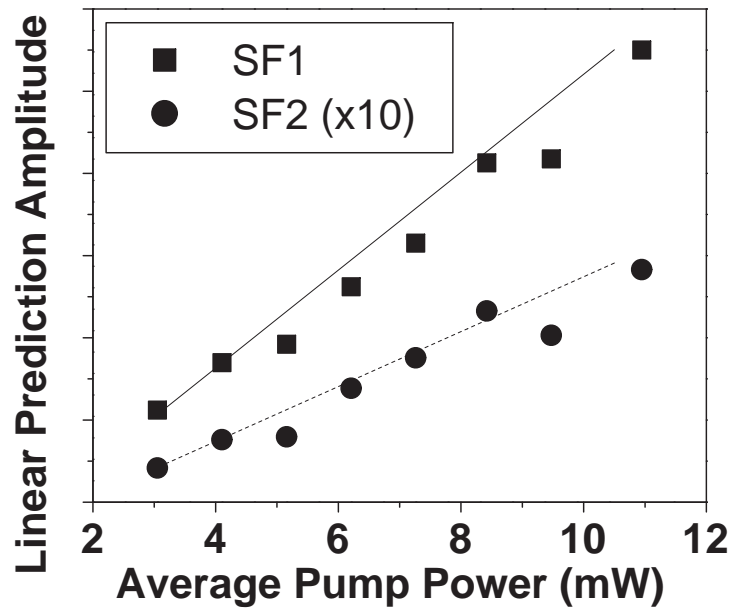

Figure 3.4 Amplitude of the single and double spin flips as a function of pump power.
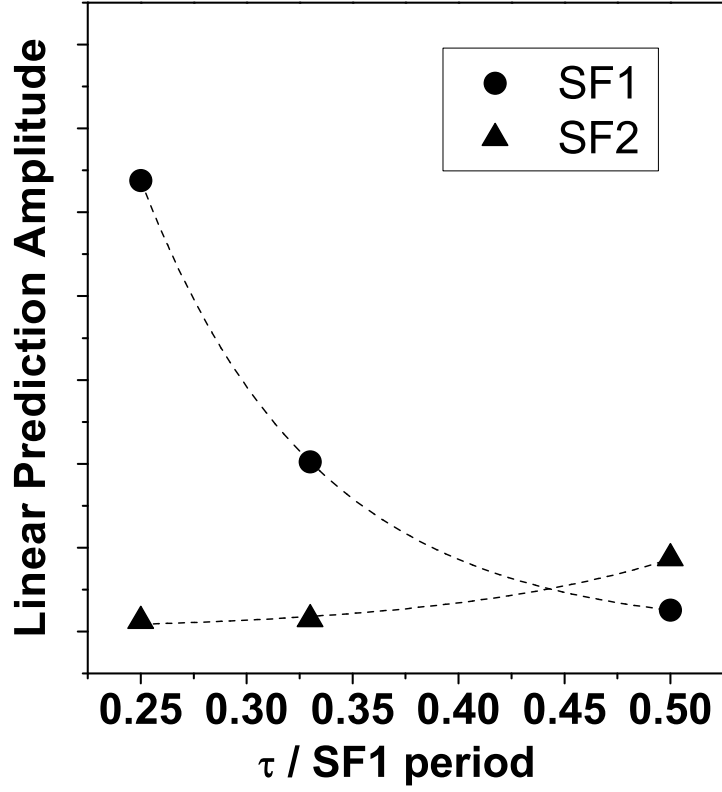
Figure 3.5 Signal of the single and double spin flip as a function of time separation between the pump pulses.

introduction of a second pulse at time τ can create a state written as,

$$\Psi = C_{-1}e^{-iE_{-1}t/\hbar}\,|-1\rangle + C_0 e^{-iE_0 t/\hbar}\,|0\rangle + C_1 e^{-iE_1 t/\hbar}\,|1\rangle$$
$$+ C_0 e^{-iE_0(t+\tau)/\hbar}\,|0\rangle + C_1 e^{-iE_1(t+\tau)/\hbar}\,|1\rangle + ex. \tag{3.6}$$

From this equation, if the energies are known, the optimal τ for enhancement or destruction of that state can be determined. We can create such a pair of pulses separated by τ using the pulse shaper. The dependence of the SF signals on τ is demonstrated in Fig. 3.5. As expected from Eqn. 3.6, as τ approaches half the period of SF1, the signal approaches a minimum while the SF 2 signal is constructively enhanced.

Additionally, since our signal decays within a few oscillations, the relative intensity of the first and second pulses must be adjusted. We do this by taking advantage of a consequence of pulse shaping using the spatial light modulator in our setup. From Nelson, (8) the output of the pulse shaper is expressed as,

$$e_{out} \propto \sum_n c_n e_{in}(t + n\beta)e^{(x+n\chi)/a^2} \tag{3.7}$$

demonstrating that an ideally arranged pulse shaper introduces spatial shift between pulses that are delayed in time by $n\beta$ and the displacement in horizontal space, given by $n\chi$ with the constants β and χ determined by the lenses, gratings, and alignment of the pulse shaper and the wavelength of the pulse shaper. The pump pulse spot's diameter in our experiment, however, is greater than the separation between the two pump pulses. This creates a gradient of relative intensities spatially across the sample as shown in Fig. 3.6. The spot measured depends on the smaller probe's location within this gradient. When the location of the probe on the pump's gradient, and the length of τ is optimal, the result is the time domain trace in Fig. 3.2 labeled two pulses. The 2 SF signal is clearly visible without the SF signal. As either the probe spot is moved away from the optimum position, or τ is adjusted away from the optimal time, cancellation of the harmonic signal becomes incomplete.

The degree of entanglement is determined from the ratio of the amplitude of the spin flip signals (16). The ensemble average, $\rho(m) = \sqrt{\sum_\eta |\langle\phi|\rho_\eta(m,0)|\phi\rangle|^2 / N_m}$, gives a measure of the entanglement. Because the amplitude of the mth harmonic is proportional to $|\rho(m)|$, the amplitude is also related to the degree of entanglement. There are N_m sets of spins, with each one labelled η. In the previous work, the ratio of amplitudes of the double and triple spin flip to the single is 0.014 and 0.46 (53). In the measurements described in this chapter, only the second harmonic was studied. The ratio of the double spin flip to the single spin flip with a single pump pulse is given by 0.049, slightly larger than before. For the ideal intensity ratios of the pulses ($I_2/I_1 = 0.69$), the ratio is 1.66. This demonstrates a clear re-
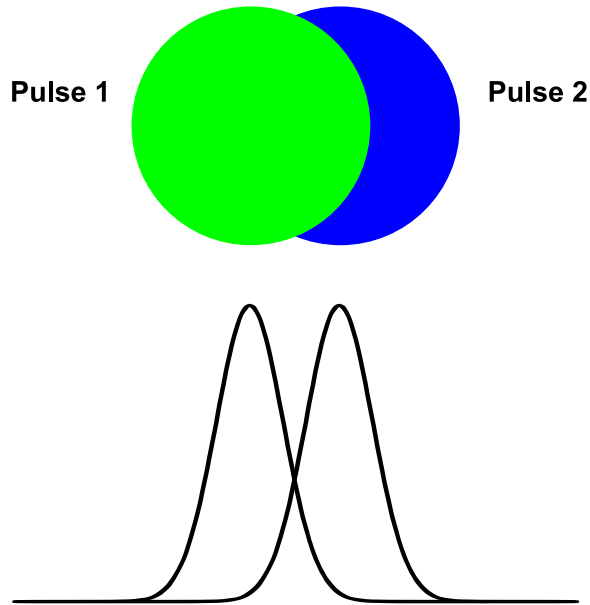
Figure 3.6   Overlap of the two pump pulses and profile of the pulse intensity across the spots.

lation between the intensity ratios of the pulses and the degree of entanglement achievable. Therefore, the separation between pulses τ or the intensity ratio I_2/I_1 controls the degree of entanglement from nearly zero to a maximum of 1.66 under optimal conditions.

3.5   Inelastic light scattering measurements

Spontaneous inelastic scattering is useful for investigating magnetic excitations in CdMnTe quantum wells (63; 64). The scattering signal from the sample detailed earlier was very strong, rivalling the amplitude of the photoluminescence from the quantum well when in resonance. This behavior, however, is dependent on the wavelength of the exciting laser. There are several electronic transitions in this sample. The photoluminescence and PLE indicate the band-edge transition involving bound heavy hole excitons at 1.68 eV (29). The excitons are bound to impurities in the well and variations in the well's barrier. At 1.69 eV in the PLE data, the free exciton transition is visible, and the band to band transition is at 1.70 eV. Above that energy, at 1.72 eV, is the light hole valence band to conduction band transition (non-degenerate with the heavy hole state due to confinement and strain

effects). While in ISIS measurements the spectral width of the pulses include all the heavy hole excitonic transitions, in SIS we can selectively excite them due to the narrower exciting spectrum. However, while the cross-section increases in resonance with real electronic transitions, the absorption also increases. This results in a smaller scattering volume. Once the laser energy moves above the band edge transitions, all SIS from spin flips becomes too small to be observed.

Our CdMnTe is zincblende and normally part of the T_d symmetry group. However, confinement in the growth direction reduces it to D_2d symmetry. The SIS measurements here were conducted to observe the anti-symmetric A_2 modes with a scattering tensor in the form of (25),

$$R_S = \begin{pmatrix} 0 & c & 0 \\ -c & 0 & 0 \\ 0 & 0 & 0 \end{pmatrix} \tag{3.8}$$

which gives us the polarization of the scattered light according to $e_S = R_s e_I$, where e_S is the scattered polarization and e_I is the incident polarization. Therefore, all the measurements were done in a cross-polarized measurement with the incident and scattering polarizations orthogonal.

For spin flip excitations, the scattered amplitude of the nth harmonic can be determined from (63)

$$P_n(\tau) = \frac{1}{\tau} \int_0^{infinite} e^{-t/\tau} \frac{N(t)^n}{n!} e^{-N(t)} dt \tag{3.9}$$

where τ is the exciton lifetime and $N(t)$ is the average change of the magnetic ion spin and is given by $N(t) = \int_V dV n'_{Mn} S \sin^2 S(1 - cos(w_L t))$ where n'_{Mn} is density of Mn ions, S is the spin of the Mn and w_L is the Larmor frequency in the effective field B_{eff}, given by

$$\omega = (B_{ext} - \frac{\kappa J}{g\mu_B}) g_{eff} \mu_B / \hbar \tag{3.10}$$

Multiple Mn spin flips are seen in the scattering data, as shown in Fig. 3.7 (63; 64).
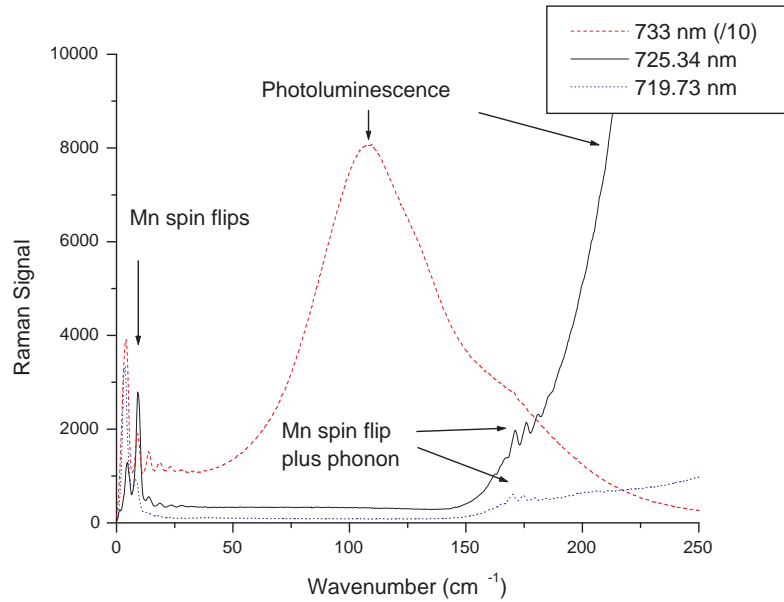
Figure 3.7 SIS data at three exciting laser energies showing the multiple spin flips of the Mn d electrons, the combined phonon spin flip modes and the photoluminescence.

The scattering is all measured cross-polarized. The broad peak seen in the spectrum is the photoluminescence at 740 nm. As the laser moves across the photoluminescence to higher energies above the quantum well's exciton resonance and bandgap, it is possible to observe more harmonics of the spin flip. The strength of the scattering reaches a maxima with the laser in resonance with the bound exciton (29). At higher energies, however, a second maxima appears. The resonance behavior of the spin flip harmonics is shown in Fig. 3.8. There is a broad peak centered at 730 nm. This is likely due to resonance with the free HH excitons. As the laser continues to higher energies and away from resonance, the signal shows only a single very strong peak indicating the single Mn spin flip. In addition to the multiple Mn spin flips, there is another series of peaks near 168 cm^{-1}. These peaks correspond to the combined LO phonon plus spin flip mode. It shares the resonance properties and selection rules of the Mn spin flips and also displays multiple spin flips.

We have studied the temperature dependence of the Mn overtones as well. While the single spin flip is independent of temperature, the overtones are highly sensitive to it and
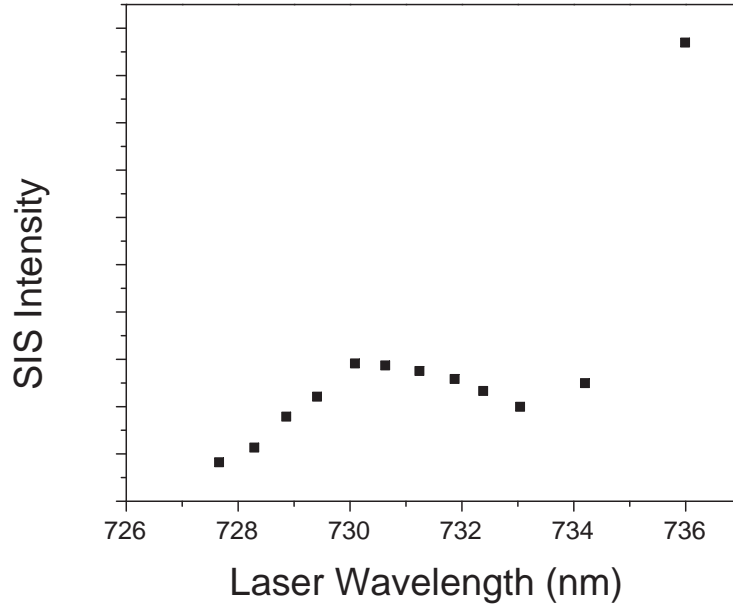
Figure 3.8 Intensity of multiple Mn spin flip peaks in SIS data as a function of exciting wavelength.

rapidly diminish at higher temperatures, totally vanishing by 20 K. This is expected as the increase in temperature rapidly randomizes the spin population. The average Mn spin, $\langle S_z \rangle$, is given by the temperature dependent Brillouin function and reflects this.

3.6 Further work

Our experiments focussed on a single sample provided to our research group. Further optimizations allowing entanglement and manipulation of additional spins may be accomplished if the formation of the bound electrons is more precisely controlled. Additionally, because the Mn concentration relied only on Mn diffusion into CdTe layers, samples with more uniform Mn distribution may also prove to have longer lived observable excitations.

Alternately, one can reduce the area of the sampled spot on the sample to reduce the inhomogeneities measured. Using a microscope objective or a mask may provide such

an opportunity, however, the laser power density must be kept sufficiently low to avoid heating. As a result, the signal may be beyond our current detection capabilities.

Chapter 4

Collective modes in CdMnTe quantum wells

4.1 Introduction

The CdTe material system provides an optimal system for studying the properties of dilute magnetic semiconductors. Manganese introduced into the CdTe lattice behaves as a column 2 element, replacing Cd. As such, it behaves as an alloy, not a dopant as in the GaAs system. Recent developments in crystal growth technique have allowed the creation of high quality CdTe quantum wells (65). With modulation doping, a high mobility 2D electron gas is formed in such a high quality quantum well. Collective modes were observed previously in GaAs quantum wells; As described in Chapter 2, oscillations of electron charge and spin have been previously observed using SIS and pump-probe spectroscopy (15; 38; 66).

Earlier photoluminescence and SIS studies have demonstrated the collective spin flip and the single particle spin flip in the high mobility 2D electron gas formed in CdMnTe quantum wells (67). From study of such excitations, important details of the dilute magnetic CdMnTe system are determined. Such information includes the spin polarization, carrier concentration, Fermi energy, Zeeman splitting, and Mn concentration. Comparing the behavior of the collective and single particle spin flips provides information on the electron interaction within the 2DEG.

This chapter will study the lifetime behavior and generation mechanism of the collective spin flip mode in a very high quality CdMnTe quantum well. First, we will cover the theory of collective mode excitations and spin decay in dilute magnetic semiconductors. Next, the SIS data taken earlier on our samples by Cynthia Aku-Leh is reviewed. Finally, we will demonstrate the effect of laser heating, Mn concentration, magnetic field, and photon energy on the lifetime of the spin flip wave.

4.2 Theory

4.2.1 Collective Spin Modes

Collective spin modes have been observed previously in GaAs (15; 19; 68). Their behavior is described by the local spin density approximation theory (69). However, the presence of magnetic impurities in our 2DEG system makes two alterations to the situation explored in these earlier works (70). Instead of the spin density excitations involving the sublevels due to the confinement of the quantum well, the levels involved are magnetic subbands split by an external magnetic field. Therefore the energy of the excitations can be controlled by the external magnetic field. Also, whereas the GaAs 2DEGs have little spin polarization, the presence of magnetic impurities in the quantum well produces a pronounced spin polarization at low temperature when an external magnetic field is applied as discussed previously.

Despite these differences, the spin density waves in GaAs and collective oscillations in CdMnTe 2DEGs show similar behavior and can be explained with the same formalism. The polarizability from the spin-flip transition can be given as,

$$P(\omega,q) = \frac{P_0(\omega,q)}{1 - V_{XC}(q)P_0(\omega,q)} \tag{4.1}$$

where $P_0(\omega,q)$ gives the non-interacting polarization in the absence of electron interac-

tions, and $V_{XC}(q)$ gives the exchange interaction between the electrons (70). The non-interacting polarization, $P_0(\omega, q)$ is seen by the behavior of the single particle spin flip (in GaAs this is the single particle excitation). The energy edges of this excitation are given by $E = g^* \mu_B \langle S_z \rangle \pm \hbar v_F q$ with g^* the effective g-factor, $\langle S_z \rangle$ the average Mn spin, v_F the Fermi velocity of the 2DEG, and q the photon wave vector. For GaAs quantum wells (69), V_{XC} in the local spin density approximation is given as,

$$V_{XC} = -\frac{0.4073}{n}[\frac{1}{r_s} - 0.036 - \frac{1.36}{1 + 10r_s}] \times R_y^* \frac{1 + (0.297\frac{r_s}{n})^2}{[1 - (0.297\frac{r_s}{n})^2]^2} \tag{4.2}$$

where n is the 2DEG electron density, $r_s = (\frac{3a}{4\pi n})^{\frac{1}{3}}/a_B^*$, a_B^* is the effective Bohr radius, R_y^* is the effective Rydberg energy, and a is the average width of the electron density in the 2DEG.

4.2.2 Decay

Conduction band electrons in magnetic semiconductors have a variety of spin relaxation mechanisms. Many of the basic spin relaxation methods in non-magnetic semiconductors were suggested over 25 years ago. More recent advances allowing high quality magnetic semiconductors have opened up the study of new decay routes as well involving the magnetic impurities.

Three primary relaxation mechanisms are responsible for spin decay in non-magnetic semiconductors. The strength of the individual mechanisms, which plays the dominate role in a given sample, depends mostly on the carrier density and temperature. First, proposed by Elliott and Yafet (EY), is a method of spin relaxation due to the Bloch states being a superposition of spin states rather than pure states (71). As a result, any scattering between Bloch states that occurs may flip the spin. This mechanism dominates in very low

temperature, n-type semiconductors. The spin relaxation rate is given by,

$$\frac{1}{\tau_s^{EY}} = A(\frac{k_B T}{E_g})^2 \eta^2 (\frac{1 - \eta/2}{1 - \eta/3})^2 \frac{1}{\tau_p} \qquad (4.3)$$

where E_g is the band gap, τ_p is the momentum relaxation time, and $\eta = \Delta/(E_g + \Delta)$ where Δ is the spin-orbit splitting of the valence band (72). A varies between 2 and 6 depending on the material, and can usually be fit from experimental results.

The most common spin relaxation method is the D'yakonov-Perel (DP) mechanism, as it dominates in all semiconductors at high temperatures (and in most cases at room temperatures) (73). The DP mechanism results from the lifting of the conduction band degeneracy for nonzero k values. The spin precesses about its own effective magnetic field. Scattering will cause k to change randomly, thus randomizing the spin as it precesses around the changing effective magnetic field. The spin relaxation rate is given by,

$$\frac{1}{\tau_S^{DP}} = Q\alpha^2 \frac{(k_B T)^3}{\hbar^2 E_g} \tau_p \qquad (4.4)$$

where Q ranges from 0.8 to 2.7 and α characterizes the non-parabolic behavior of the conduction band electron momentums (72). Introduction of a magnetic field tends to suppress the DP mechanism (74).

The final process common in non-magnetic semiconductors is the Bir-Aronov-Pikus (BAP) mechanism involving holes (75). It dominates at low temperatures in p-type semiconductors with large hole concentrations. Both recombination and exchange between the electron and hole spins are taken into account. The spin relaxation rate is given by,

$$\frac{1}{\tau_S^{BAP}} = \frac{2a_B^3}{\tau_0 v_B} (\frac{2\varepsilon}{m_c})^{1/2} (n_{a,f} |\psi(0)|^4 + \frac{5}{3} n_{a,b}) \qquad (4.5)$$

where $n_{a,f}$ and $n_{a,b}$ are the concentration of free and bound holes with the other values are given in reference (72). It is worth noting that for our sample, the hole spins in the CdMnTe

layer are not aligned with the external magnetic field. As discussed in the previous chapter, spin-orbit coupling constrains them perpendicular to the well (56; 57; 58; 59).

With the introduction of a magnetic field and magnetic ions, new routes of spin relaxation are introduced and the significance of the previous methods may be altered. The first new mechanism involves variations in the local g-factor, which has been referred to as the variable g-factor (VG) spin relaxation (74). The random introduction of Mn as an alloy in the lattice leads to such a variations as electrons experience different local Mn concentrations as they move. The decay rate is given by,

$$\frac{1}{\tau_{VG}} = \frac{\gamma^2 \tau_0}{N_{ex}} (n_0 x k_B T \chi(B,T) + \langle M_z \rangle^2 + \frac{n_0 x k_B T (3 * \chi(0,T) - \chi(B,T)) - \langle M_z \rangle^2}{2 + 2(g_0 \mu_B B/\hbar + \gamma \langle M_z \rangle)^2 \tau_0^2}) \quad (4.6)$$

with $\gamma = J_{sp-d}/(n_0 g_{Mn} \mu_B \hbar)$, τ_0 the interaction time between locations of differing Mn spins, N_{ex} is the number of Mn involved, x is the percentage Mn concentration, n_0 is the lattice cell density, T is the temperature, $\chi(B,T)$ is the susceptibility, $\langle M_z \rangle$ is the average magnetization along the external field, and g being the related g-factors (76). The constant, J_{sp-d} is the coupling between the Mn d electrons and the conduction band electrons.

Introduction of Mn also leads to another scattering method called exchange scattering (77; 78). The s-d interaction between the electrons and Mn spins can result in a spin flip. The scattering time for quantum wells can be given by,

$$\frac{1}{\tau_e} = \frac{35}{8} m^* (N_0 \alpha)^2 x_{eff} / \hbar^3 L_W N_0 \quad (4.7)$$

with m^* the effective mass, x_{eff} the concentration of Mn, N_0 the cation sites per unit volume, L_W the quantum well width, and $N_0 \alpha$ the same exchange integral that has been mentioned previously.

All of these scattering mechanisms are, to varying degrees of importance, present in our sample. The EY mechanism tends to dominate only when the other mechanisms are not present at the lowest temperatures and longest lifetimes. The DP mechanism dominates

41

at higher temperatures above the liquid He immersion conditions of our experiments. The BAP mechanism requires many holes, which are normally present only in small numbers due to n-type modulation doping in our quantum wells, however, the optical pulses absorbed by the well generate non-equilibrium electron-hole pairs. The VG and exchange scattering methods are both also present due to the incorporation of Mn. Because the system is paramagnetic, it rapidly becomes disordered with rising temperature. This disorder manifests as a reduction in lifetime through the VG and exchange scattering mechanisms.

4.3   Material System

The samples have a high mobility, MBE grown $Cd_{1-x}Mn_xTe$ quantum well sandwiched between CdMgTe barriers, as shown in Fig. 4.1 (65; 79). The primary sample used here has a Mn concentration of 0.75%, although for comparison a second sample with a 0.46% composition was also measured. In the barrier 200 Å above the quantum well is a layer of Iodine modulation doping. Iodine dopants in CdMgTe barrier layers lack the deep defect levels formed by In doping in the last chapter, and can create layers with up to $5 \times 10^{19} cm^{-3}$ carriers at room temperature (80). These carriers diffuse into the quantum well, and act as a 2DEG (81). The electron density in the quantum well is $2.9 \times 10^{11} cm^{-2}$. The presence of these n-type carriers raises the Fermi energy of the quantum well above the lowest conduction band state as shown in Fig. 4.1.

In an applied magnetic field, the Mn d electron spins in the quantum well align along the field. The exchange interaction between the Mn electron spins and the conduction band electrons also strongly aligns the conduction band electron spins with the field (82). This results in a large Zeeman splitting of the conduction band. This splitting causes a net spin polarization and a large g-factor for the conduction band electrons. At the energies of interest in this work, only the lowest conduction subband of the quantum well plays a role.

The photoluminescence and photoluminescence excitation data taken by Cynthia Aku-
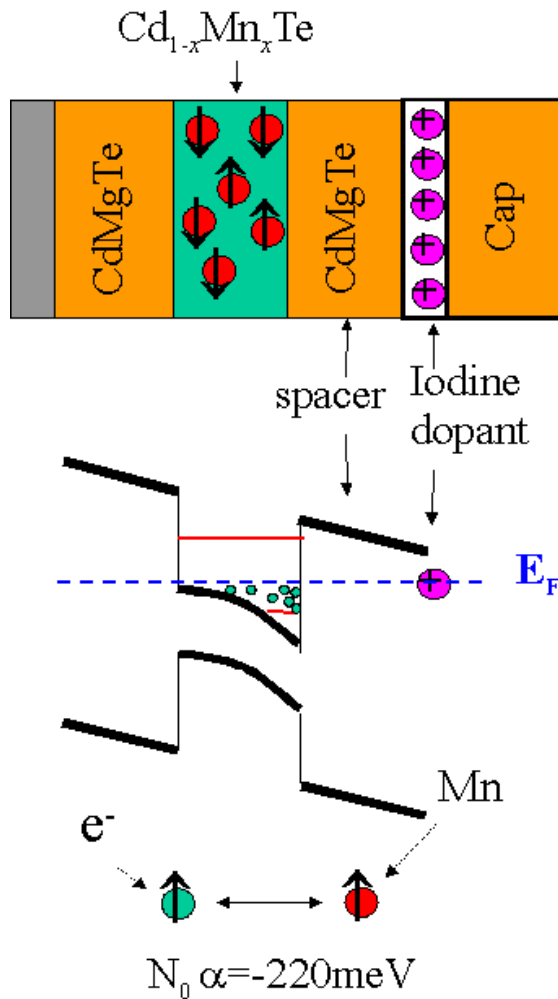
Figure 4.1 Two dimensional electron gas in a CdMnTe quantum well. The structure is shown at the top, with the corresponding band structure below. E_f indicates the Fermi level.

Leh for the samples studied are shown in Fig. 4.2. The lowest energy of the photolumi-nescence peak centered at 1.607 eV is the conduction band edge to valence band transition for the 0.75 % sample used in most of the experiments. The high end of the photolumi-nescence peak at 1.617 eV is the transition from the valence band to the unoccupied levels at the Fermi energy within the conduction band. The photoluminescence excitation above 1.617 eV represents the absorption of the sample. The lowest energy peak is the transition between the valence band and the unoccupied states at the Fermi energy in the conduction

band. The higher energy peaks are the transitions to excited conduction and valence band sublevel states within the well. The similar PL and PLE data for a lower Mn concentration sample used in a few experiments are shown in the lower half.

The selection rules of the photoluminescence are shown in Fig. 4.3. The σ_0 and π_1 peaks indicate transitions between the band edges involving Zeeman split states aligned with the external field. The σ_1 and π_0 peaks are transitions between the bands with spin states opposite the field. The presence of the σ_1 and π_1 peaks in the data at intermediate fields is due to mixed spin states in the valence band. The separation energy between the σ_0 and σ_1 peaks and the π_0 and π_1 peaks is the Zeeman energy of the conduction band electrons, given by $Z = -N_0 \alpha x \langle S_z(B,T) \rangle$ with the average Mn spin $\langle S_z \rangle = S_0 B_{5/2}\left(\frac{(5/2)g\mu_B B}{k_B(T+T_0)}\right)$ with $g = 2$ for the Mn spin system, x the Mn fraction, N_0 the number of unit cells per volume and α the exchange integral (55; 79). The highest edge of the photoluminescence, σ_{edge} and π_{edge}, represent the highest occupied energy state at the Fermi energy.

4.4 Spontaneous Inelastic Scattering Studies

Earlier SIS experiments have studied the collective and single spin flip modes in the same CdMnTe quantum wells used in the studies here (70; 79; 83). Data from these SIS measurements is shown in Fig. 4.4. First, they demonstrate the expected wave vector dependence of both modes as shown in Fig. 4.5. The k-vector dependence of the single particle spin flip follows the expected trend, $E_z \pm \hbar(2\frac{E_f}{m^*})^{0.5}q$ where E_z is the Zeeman splitting and E_f is the Fermi energy. The spin flip of a single electron expands with wave vector from a single energy into a continuum of levels. The collective spin wave remains a single state, but at sufficient wave vector, it merges with the single spin flip continuum. The signals from both excitations display a Brillouin function dependence on magnetic field, as shown in Fig. 4.4. The spin wave is the narrow peak at lower energy. The spin flip appears at higher energy as a broad peak, suggesting the continuum nature of the excitation. These
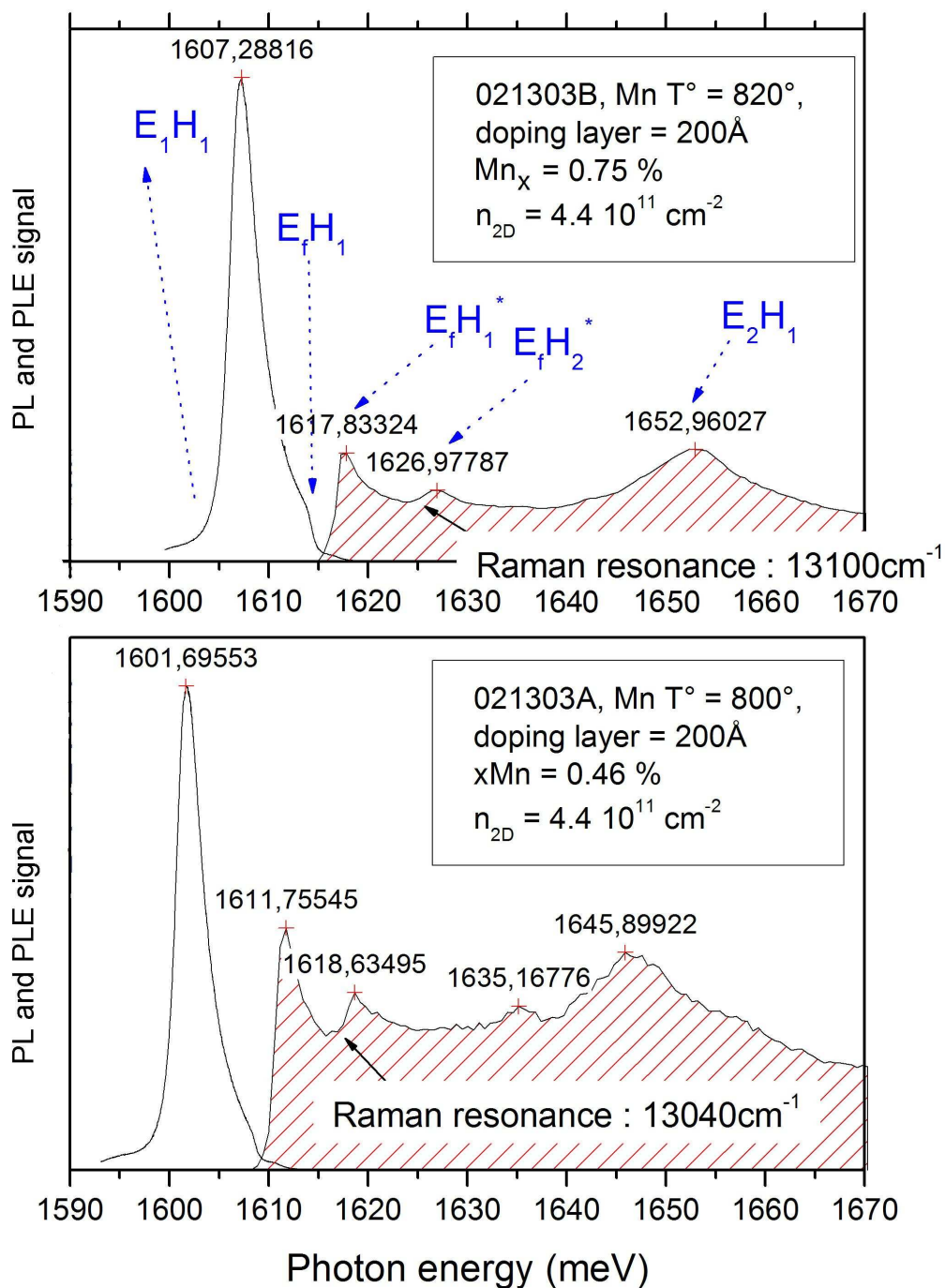
44

Figure 4.2 Photoluminescence and photoluminescence excitation data from the samples. The unfilled curve to the left is the PL data, and the shaded region on the right is the PLE data. Transitions between states are marked by crosses.
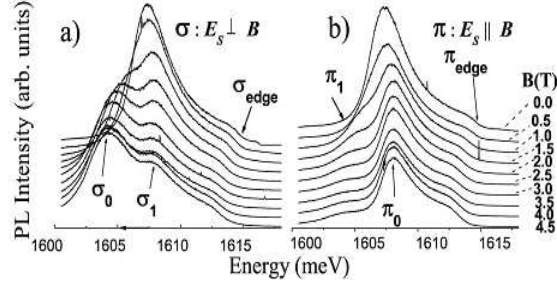
Figure 4.3 Selection rules of the photoluminescence for both magnetic field orientations, from (79). The σ and π transitions indicate transitions between Zeeman split states.
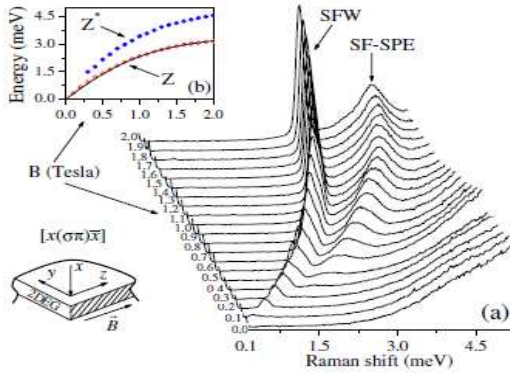

Figure 4.4 Inelastic scattering data indicating the magnetic field dependence of the spin wave (SFW) and spin flip modes (SF-SPE) at many wavelengths, from (79).
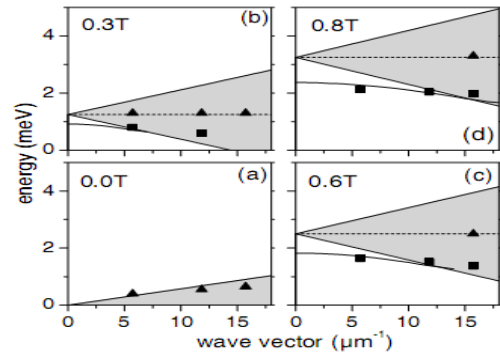

Figure 4.5 Inelastic scattering energy calculations of the spin wave (solid line) and spin flip (shaded region) on the exciting wave vector. The squares and triangles indicate SIS data for four magnetic fields, from (70).

SIS measurements, like the ultrafast measurements detailed in the next section, were done in a backscattering geometry, so $q \approx 0$ and the spin flip wave and single particle excitations have differing energies.

The SIS data have also shown a strong dependence on laser excitation power through the temperature dependence of the Brillouin function. The energy of the spin flip is related to the average Mn spin by,

$$E = N_0 \alpha x \langle S_z \rangle \tag{4.8}$$

where $\alpha = \langle S | J^{sp-d} | S \rangle / \Omega_0$ (2). This is the sp-d exchange integral divided by the volume Ω_0. N_0 is the number of cations per volume. The α is the exchange integral, x is the Mn concentration, and $\langle S_z \rangle$ is the average Mn spin. For the CdMnTe system, $N_0 \alpha$ is 0.22 eV.

46

The average Mn spin is given as,

$$\langle S_z \rangle = A_0 B_{5/2} \left(\frac{\frac{5}{2} g \mu_B B}{k_B (T + T_0)} \right) \tag{4.9}$$

where $B_{5/2}$ is the Brillouin function, g is the g-factor, μ_B is the Bohr magneton, B is the applied magnetic field, k_B is the Boltzmann constant, T is the temperature, and T_0 accounts for the antiferromagnetic coupling between neighboring Mn atoms. The temperature and magnetic field dependence of both excitations are given by this curve.

4.5   Inelastic Scattering

The experimental pump-probe measurement setups used on the CdMnTe quantum well samples are described in chapter 2. While some details varied by experiment, most of the measurements done here used a circularly polarized pump to excite a single spin orientation. The probe was linearly polarized and backscattered at a nearly normal incidence. The polarization rotation of the reflected probe was measured using a balanced detector. Unless specified otherwise, the pulse was 100 fs long and centered at 768 nm. The external magnetic field was applied to the sample in the plane of the well at 2 T. The samples were always immersed in liquid He and pumped on to achieve temperatures below 2 K. Maintaining He immersion was crucial due to the effects of temperature described later in this section. An example of the pump-probe data observed under high laser fluence with the corresponding linear prediction fit spectrum is shown in Fig. 4.6(a), and for lower power in Fig. 4.6(b). The spin flip wave is the single peak shown in the low laser fluence spectrum. The four peaks in the high fluence are all spin flip wave oscillations from different regions of the laser spot, as discussed later.

The pump-probe data is presented in three sections. The first factor responsible for decay of the spin flip wave is heating. While the sample can be heated externally, in this case the laser absorption acts as the thermal source. At even modest laser powers, heating
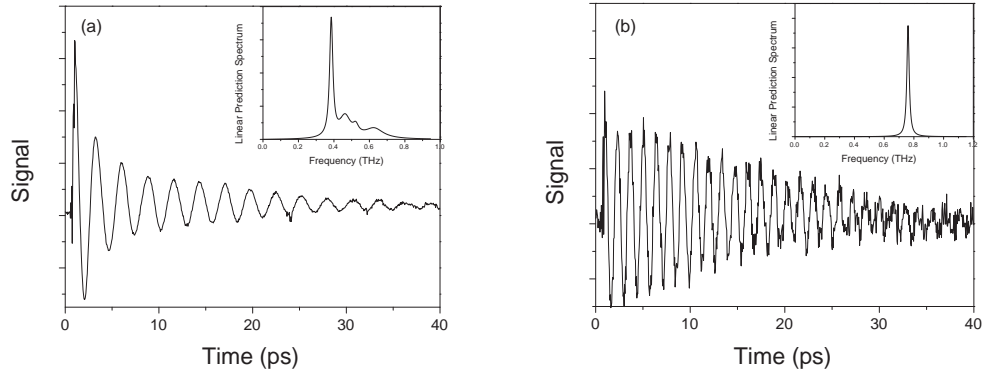
Figure 4.6 Pump-probe data showing the spin flip wave and its spectrum taken under high (a) and low (b) laser fluence. The multiple peaks shown in the high power data represent zones of elevated temperature. The single particle spin flip is not observed in either case.

dominates as the deciding factor in the lifetime, and results in the formation of multiple zones of temperature. With sufficiently low laser powers, however, the lifetime becomes a function of the number of photoexcited carrier. As the laser moves into resonance and excites more carriers, the lifetime decreases. Finally, the effects of magnetic field, and Mn concentration, which both relate to spin polarization, are demonstrated. Both counteract the effect of temperature, resulting in longer lifetimes with increasing Mn concentration and magnetic field.

4.5.1 Thermal Effects

We have studied the behavior of the spin flip wave in 2DEG systems in the time domain under a variety of conditions. The first experimental challenge was controlling the effect of laser heating on the Mn and electron spins. We have been able to ascertain the temperature of the sample by fitting the experimentally determined spin wave frequencies as a function of magnetic field to equation 4.8. The temperature is used as the fitting parameter with all other values are known. An example of two data sets and the corresponding fitting curves are shown in Fig. 4.7 for two laser fluences. The temperatures listed assume a negligible
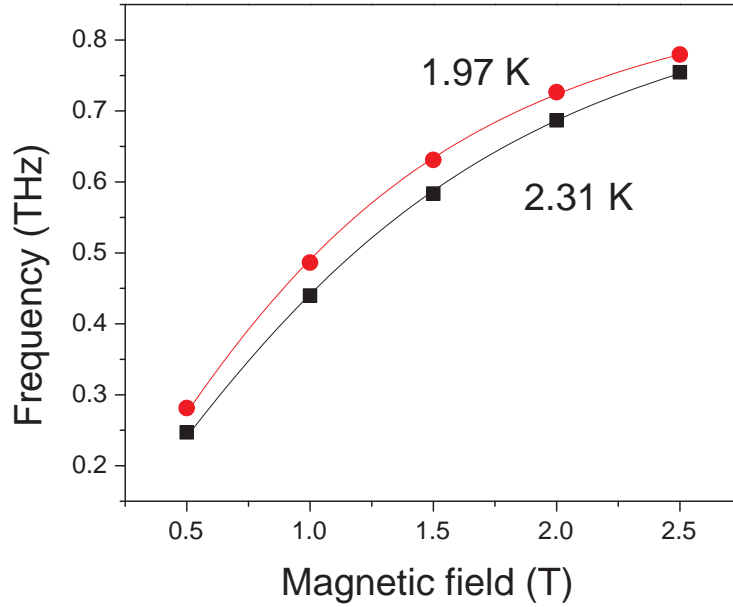
48

Figure 4.7 Frequency of the spin flip wave with magnetic field and corresponding fits to the Brillouin function. The two curves were taken under differing laser fluence. The temperature used for the fit is shown.

value for T_0, a reasonable assumption given the low Mn concentration in the samples.

As the energy of the exciting photons rises above the bandgap, more heat is produced due to increased absorption. Optically excited electrons decay to the lowest unoccupied state, releasing energy, which becomes heat. Shown in 4.8a, at higher laser powers heating takes place in the form of the creation of regions of higher temperature (84; 85). As the Mn in the lattice heats, the spin relaxation process accelerates creating a feedback loop with instabilities. Areas where laser heating is sufficient to create such instabilities can be identified in our data by the frequency of the spin flip wave, which depends on the temperature as described by the Brillouin function. The spin flip wave's frequency in these regions approaches the coldest temperature region's spin flip wave frequency as the laser power, and therefore the temperature, is lowered. These regions merge into a single zone with the laser power in the 0.3 to 0.4 mW power range (with a 100 micron spot size). Above 2 mW, the coldest region begins to increase in temperature. The higher energy regions all show sim-
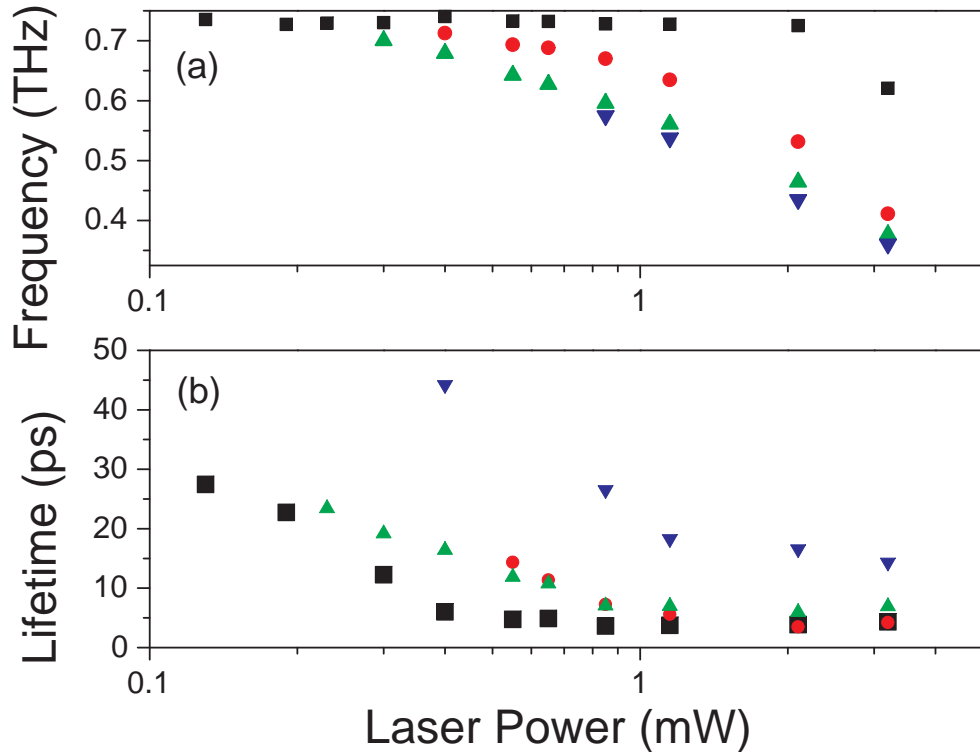
Figure 4.8 Power dependence and lifetime of the collective spin mode frequencies (a) and lifetime (b) taken in He immersion with a constant probe power of 100 μW at 768 nm with a pulse width of 100 fs and an externally applied field of 2 T in the plane of the well. The top line of data points indicates the region of the stable, lowest temperature up to 2 mW. The coldest temperature region is denoted by squares.

ilar characteristics, but likely differ from one another due to imperfections in the quantum well, local variations in Mn concentration, or deviation from a gaussian profile of the pump or probe spots. The effect of temperature is clear in the reduction of the spin wave lifetime with increasing power as shown in Fig. 4.8b. Note that the lifetime is linearly dependent on power at sufficiently low powers where negligible heating is present.

We can demonstrate that, at sufficiently low illumination levels, the feedback loop generating high temperature regions does not begin, and only a single temperature zone is created as seen in Fig. 4.8b. In Fig. 4.9, three curves fit by the Brillouin function and taken
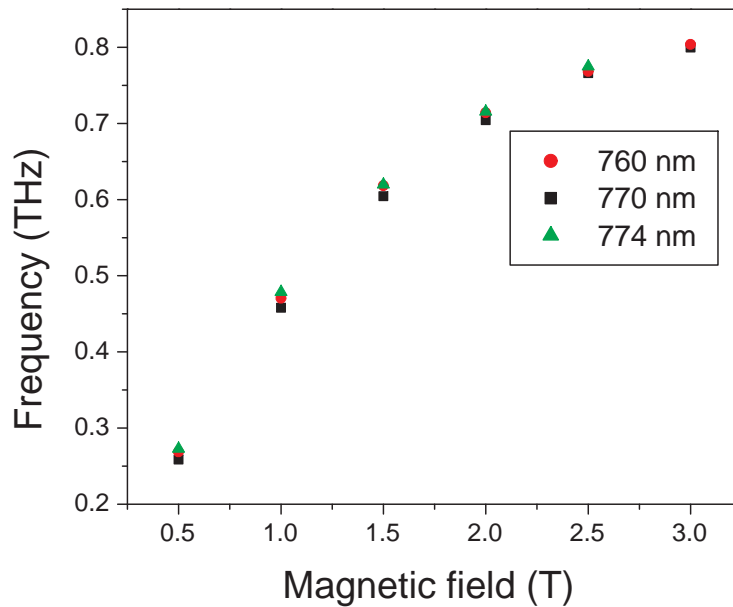
Figure 4.9 Frequency of the spin flip wave with magnetic field at three laser wavelengths. All three demonstrate similar Brillouin behavior indicating the same temperature.

with the laser at different wavelengths are shown. All three fits result in nominally identical temperatures, indicating there is no heating under this illumination level. At 774 nm, the center of the pulse energy is below the absorption edge and out of resonance although the higher energy tail of the pulse's Gaussian spectrum lies in resonance. At 770 nm, most of the central pulse energy is near resonance with the absorption edge. At 760 nm, most of the laser pulse's Gaussian spectrum is above the absorption edge. The identical Brillouin curve fits of the spin wave frequency indicate a constant temperature, independent of wavelength. With the effects of heating isolated in this way, we can examine the effect of resonance on the lifetime of the spin wave excitations independent of thermal causes.

4.5.2 Photoexcited Carriers

The lifetime behavior of the spin wave with magnetic field for the same three wavelengths is shown in Fig. 4.10. Although there is no heating at different wavelengths, the spin wave
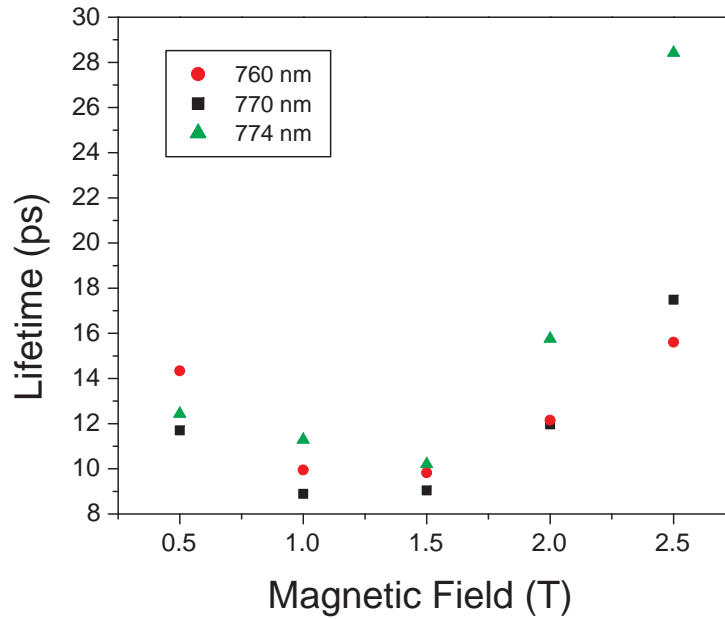
Figure 4.10 Lifetime of the spin flip wave for three laser wavelengths above, at, and below the absorption edge. As the laser moves further into the sample's absorption, the spin flip wave becomes shorter lived.

with the laser photon energy above the absorption edge appears to have a significantly shorter lifetime. Therefore, another factor is relevant to the spin lifetime. The results of 4.8b demonstrating a linear dependence of the lifetime on laser fluence at the lowest laser powers suggests that the number of photoexcited carriers plays a role. To study this relationship further, data was taken with the laser tuned across the resonance spectrum of the sample.

The amplitude behavior of the spin wave is shown in Fig. 4.11. The resonance edge is at 1.619 eV (768 nm), which corresponds to the absorption edge in the PLE data. The spin wave amplitude is clearly enhanced when the laser is in resonance with the electronic transitions as expected. The width of this resonance corresponds to that of the exciting laser pulse's spectrum. To further study the behavior around the narrow resonance, the pulse was broadened temporally to 300 fs, thus narrowing the spectral range of the pulse to 6 nm
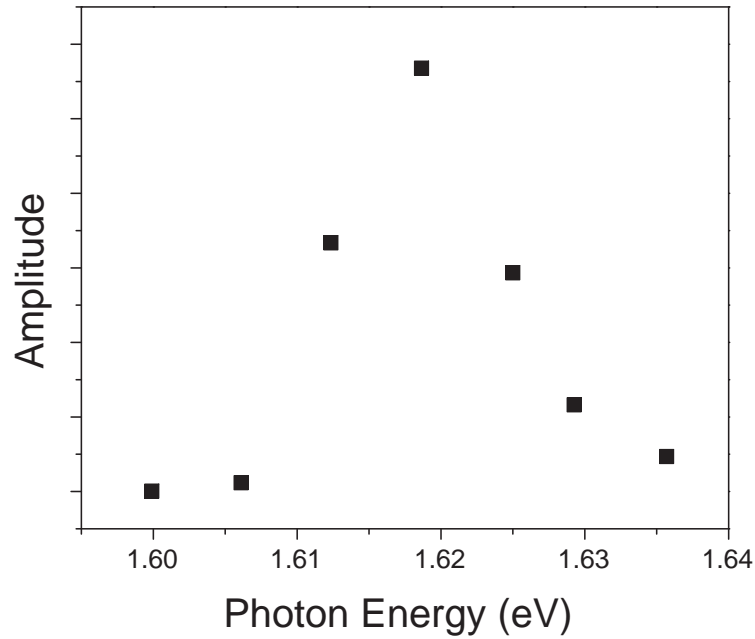
Figure 4.11 Amplitude of the spin wave with the laser near resonance. The amplitude peaks with the laser in resonance with the absorption edge.

(13.8 meV).

The corresponding lifetime behavior of the spin wave for two pulse widths with an external field of 2 T is shown in Fig. 4.12. The lifetime becomes much longer when the pulse moves toward the resonance edge. Since we have shown earlier that the temperature of the sample is not altered by the laser's photon energy under the experimental conditions used here, the strong dependence on absorption suggests that photoexcited carriers play a role in the relaxation of the spin wave. A minimum in the spin wave lifetime occurs in the spectrally narrower 300 fs pulse data with the laser wavelength at 768 nm, coinciding with one of the absorption peaks due to the valence band-conduction band transition.

With a pulse width of 300 fs and with the laser out of resonance, to the red of 768 nm, the signal becomes much weaker and requires higher laser powers to observe, which does result in heating. This heating, as mentioned before, reduces the lifetime and frequency of
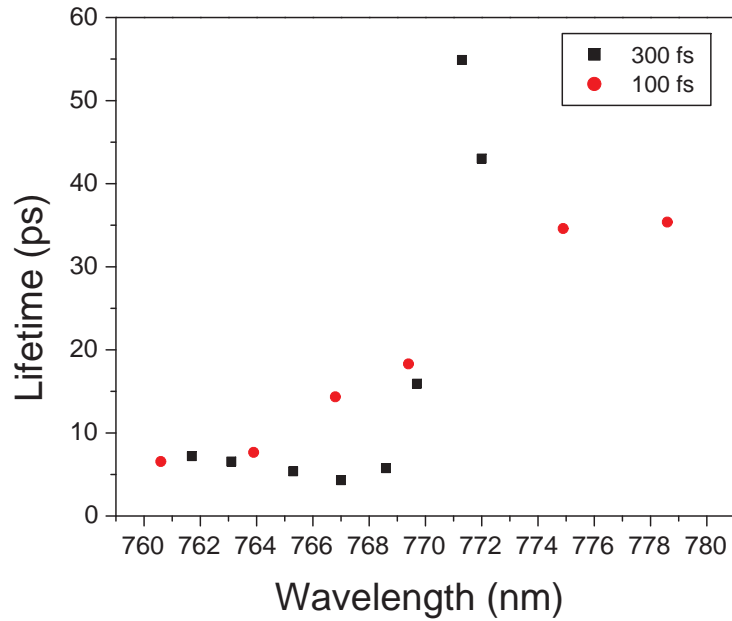
Figure 4.12 Comparison of the resonance behavior of the spin flip wave decay with two pulse widths. The spectrally narrower 300 fs pulse shows a sharper lifetime profile.

the spin wave mode. With a laser pulse width of 100 fs (18 nm FWHM), the spin wave can be observed out to a central wavelength of 780 nm. Even far out of resonance at 780 nm, the lifetime remains shorter than that of the spectrally narrower 300 fs pulse.

Photogenerated carriers can affect the spin wave lifetime through the mechanisms mentioned previously in this chapter. The carriers are not energetic enough to play a DP-style role, and the EY mechanism tends to be the weakest. The photogenerated carriers do include a substantial number of holes, which otherwise are extremely few in number. These photoexcited holes, like the ones in the previous chapter, are confined by the quantum well's boundaries, and therefore also have their spins aligned perpendicular to the external field, the electrons in the 2DEG, and the Mn ions. It is therefore most likely that a BAP spin scattering mechanism involving the photoexcited holes is responsible for the carrier effects demonstrated here.

4.5.3 Spin Polarization and Selection Rules

In addition to the effects of temperature and carriers mentioned so far, as the magnetic field increases, according to the Brillouin function, the average Mn spin aligns with the field. Because the deviation in Mn spin has decreased, as electrons travel through the material they experience less disorder. Therefore, the scattering due to local variations in the Mn spin through the VG and exchange scattering mechanisms decreases. This is demonstrated for both samples shown in Fig. 4.13. The lifetime increases with magnetic field up to the highest magnetic field available.

The effect of Mn content on the collective mode lifetime is shown in Fig. 4.13. As the previous results for the temperature and magnetic field dependence of the spin wave lifetime have shown, as the Mn spin polarization increases, the 2DEG experiences a more uniform g-factor, and therefore a slower relaxation rate. As indicated in Equation 4.8, the frequency also depends on the Mn concentration. As expected, the frequency increases with Mn concentration. This pattern should continue until T_0 becomes a significant factor due to the increasing number of antiferromagneticly coupled Mn neighbors.

In addition to studying the decay of the collective spin flip mode, we also determined its selection rules. The pump-probe data taken in differing geometries is shown in Fig. 4.14. When horizontal, the polarization of the probe is parallel to the externally applied magnetic field. The excitation and background are sensitive to the probe's polarization. The spin flip wave also is sensitive to the pump's polarization with stronger excitation for circularly polarized light where only one of the possible spin states is excited. We also measure the reflectivity of the probe instead of the polarization rotation. Under such conditions, the spin flip wave also observed, but it was weaker. The large electronic background signal indicating photogenerated carriers was also detected, making the setup less optimal for measurement.
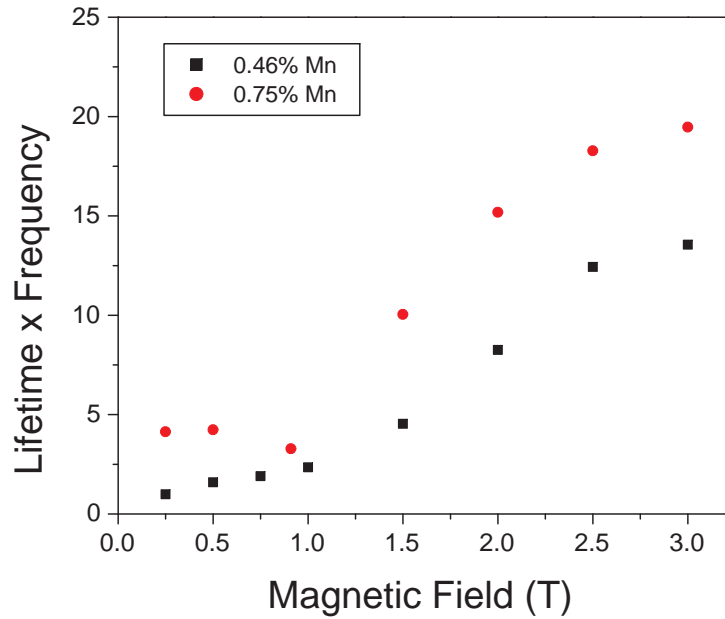
Figure 4.13 Lifetime × frequency as a function of magnetic field for two samples with differing Mn concentrations. The degree of spin polarization of the 2DEG increases with both magnetic field and Mn concentration. The lifetime here shows the same dependence on both factors.

4.6   Future Work

Further information about the decay of the collective modes can be determined by testing the system under higher magnetic fields. Because the optically excited heavy holes likely play a role and because their spins rotate toward an externally applied magnetic field, we would expect the decay to stop increasing after a magnetic field sufficient to align the heavy hole spins along the field's direction. For a more accurate measurement of the resonance behavior of the spin flip wave, ps length pulses with much narrower energy distributions could be used. The Tsunami laser we used cannot be easily modified in such a way, but other ps Ti-sapphire lasers are commercially available. Further work is also needed to identify the single particle spin flip excitation or explain the lack of it in pump-probe measurements.
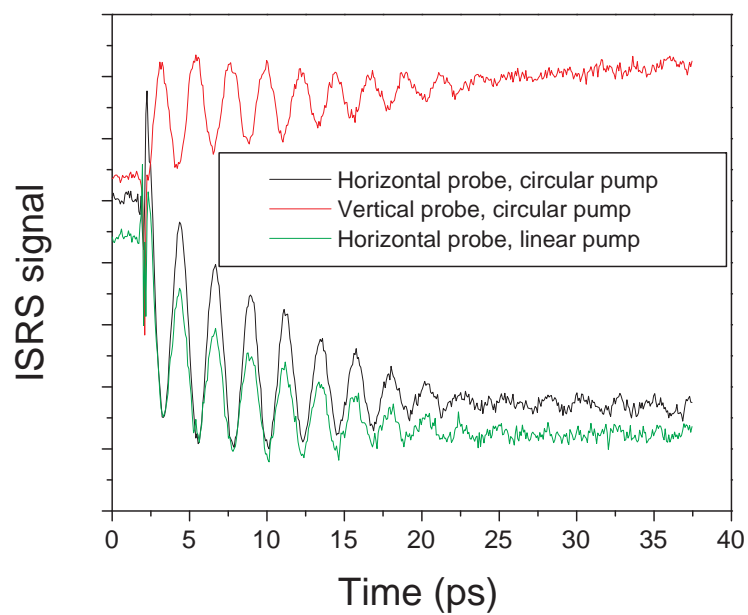
Figure 4.14 ISIS data with alternate pump and probe polarizations. The external magnetic field is along the horizontal direction.

Chapter 5

GaMnAs Ferromagnetism

5.1 Introduction

As previously mentioned, GaMnAs cannot be grown under ideal GaAs growth conditions (86). As Mn incorporation under equilibrium conditions is limited to 1%, relatively low substrate temperatures are required to incorporate substantial quantities of Mn while avoiding formation of MnAs clusters (87). As a result of the low growth temperature, the lattice contains many defects (88). Material quality has improved, however, by altering the As flux and other growth conditions to minimize defects. This has allowed ferromagnetic GaMnAs Curie temperatures and Mn concentrations to reach their theoretical limit (89; 87). The highest T_C GaMnAs samples are now around 173 K.

As in CdMnTe, neighboring Mn atoms behave antiferromagnetically. This commonly occurs when MnAs precipitates in poorly grown GaMnAs and forms clusters. The ferromagnetism in GaMnAs is mediated by the acceptor holes associated with substitutionally doped Mn_{Ga}. This process is described by theories originally designed for other systems now called RKKY theory (87; 90; 91). However, while the Mn does act as an acceptor, it is not a perfect one. The locallized defect states in the bandgap. These levels have been observed previously in several measurements studying defects in semiconductors (92). With sufficient doping, these localized defects begin to form a defect band above the GaAs valence band (93).

In this chapter, two aspects of ferromagnetism in GaMnAs will be studied, building on earlier results in the dissertation of Daimian Wang (94). First, the effect of growth conditions on the Damon-Eshbach modes was studied, specifically the effect of the As source. Second, SIS measurements of GaMnAs in a magnetic field will be discussed.

5.2 Growth Conditions

Earlier work by Daimian Wang reported on Damon-Eshbach precession modes in ferromagnetic films (95). Damon-Eshbach modes are standing spin wave modes in confined layers of ferromagnetic material (96). In the case of this work, layers of GaMnAs act as a ferromagnetic slab. The excitation mechanism to create these spin waves was similar to reported results in nickel thin films (97) where laser heating caused generation of magnons. Whereas in the previous chapter, laser heating caused the decay of magnons in our paramagnetic CdMnTe films, in the ferromagnetic GaAs discussed here, that heating is the cause of the perturbation resulting in the generation of magnons. This occurs because of the reorientation of the easy axis of the GaMnAs ferromagnet with temperature. The laser heating causes an immediate deviation of the easy axis of the ferromagnet, creating an impulsive restoring force.

We conducted pump-probe measurements on two sets of samples grown to nearly identical specifications. The measurements consisted of applying a magnetic field to the sample of 2 T for 20 minutes to align the ferromagnetic GaMnAs along the field, and then a reduction in the field to lower values. The measurements were done as described in chapter 2, with the polarization rotation detected by the balanced detector. The laser was at 800 nm, and the sample held at 5 K. All of the samples used in (95) were grown using an As cracker cell. In such a system, As_4 is evaporated from a pure As source. The evaporated As_4 is then cracked at high temperature, decomposing into As_2. An early example of a cracker cell and its function is described in a paper by Krusor (98).
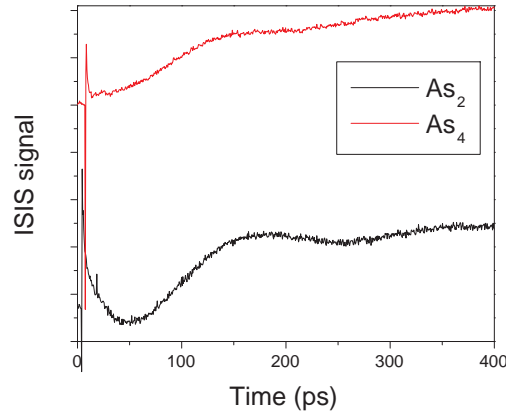
Figure 5.1 Damon-Eshbach mode oscillations in GaMnAs grown with As_2 and As_4. This data was taken at 0.13 T at 6 K.

Identical ultrafast measurements were performed on these samples grown without a cracker cell. In previous studies of structural characteristics of GaMnAs films, it has been noted that films grown with As_2 dimers grow higher quality films with higher Curie temperatures (99). The samples all consisted of 50 nm GaMnAs layers with concentrations of 2-6% Mn grown with a substrate temperature near 250 C. There was no GaAs capping layer, all samples were grown after an epitaxial, GaAs layer grown at 590 C.

Shown in Fig. 5.1 are the Damon-Eshbach oscillations in the two samples. These ISRS measurements were done as described in Chapter 2, except before taking data the ferromagnetic GaMnAs was aligned by a larger external field of 1.75 T. The two samples measured in Fig. 5.1 have similar Curie temperatures at 90 K, but the oscillations in the sample grown with As_4 has clearly weaker oscillations. At a magnetic field of 0.0875 T, the observed spin wave mode in the As_4 sample has an amplitude of 2.179E-6 V on the detector. The As_2 sample has an amplitude of 1.224E-5, about a factor of 6 larger. Similar results are obtained at other low magnetic field values, and for samples of several concentrations. Also, the higher order modes observed in (95) are not observable here in the As_4 grown sample. These findings suggest that the defects caused by the As species used, while not affecting the overall ferromagnetic behavior through the Curie temperature, do affect

the behavior of spin waves. Because the Damon-Eshbach modes are highly dependent on the surface conditions, the As species used evidently plays an important role in interface formation.

5.3   Spontaneous inelastic scattering of Mn defect states

We have also used spontaneous inelastic scattering to study bulk GaMnAs. Earlier, Daimian Wang reported on the observation of Mn-related defect levels in bulk GaMnAs (94). These energy states involve holes bound to Mn ions in the lattice. The excitation noted in SIS was the transition between the ground and first excited bound Mn state. The presence of these individual, bound hole states indicates paramagnetic regions of non-interacting Mn separated from the ferromagnetic region of the GaMnAs layers.

The excitation between ground to excited state was observed in SIS only under a narrow range of exciting laser wavelengths. Additionally, it displayed several side-peaks, as well as selection rules depending on the state of the incident and scattered light. Shown in Fig. 5.2 is a set of SIS data taken earlier demonstrating both the side peaks due to magnon scattering and the selection rules at high temperature (94). The selection rules indicated were obtained by placing a quarter wave plate before and after the sample, followed by an analyzing polarizer. Because we have already stated that the region of the bound hole transition excitation is paramagnetic, there must be an interaction between the bound hole and the nearby ferromagnetic bath for magnons to be involved in the scattering process. This is likely due to the optically formed exciton. The lower energy peak labelled 0 corresponds to the absorption of a magnon. This weakens with decreasing temperature as less magnons are available. On the other hand, the peaks labelled 2 and 3 correspond to the creation of magnons.

Earlier data indicates a dependence on the incoming scattering polarization independent of the scattered light polarization (94). This was demonstrated as a function of magnetic
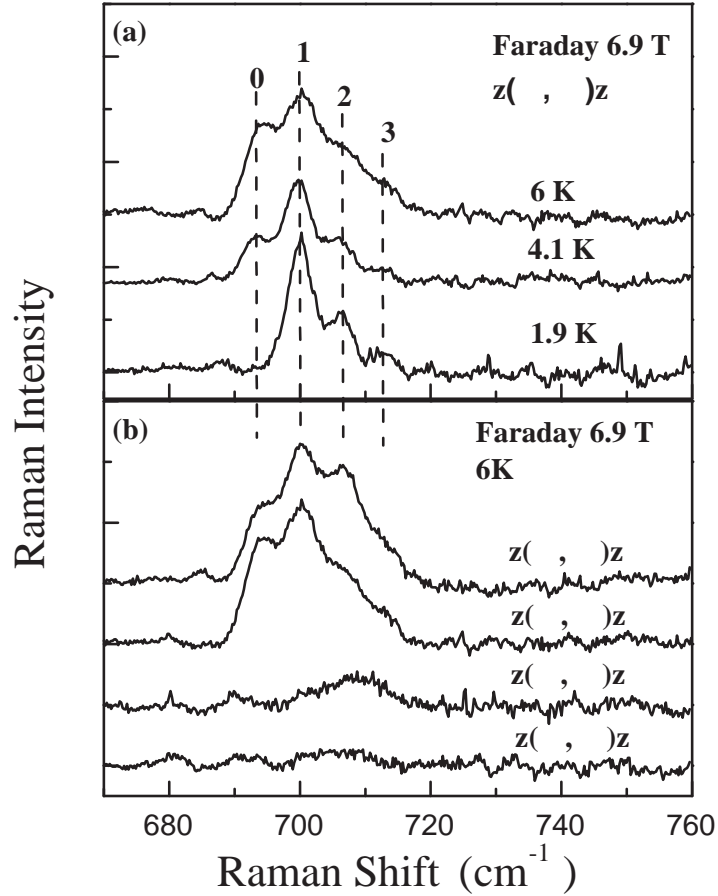
Figure 5.2 Spontaneous inelastic scattiner of GaMnAs showing transitions between bound hole states. a) Demonstration of the side peaks cause by magnon scattering. b) Selection rules at high temperature.

field for two samples in Fig. 5.3. This behavior suggested a dependence on the level population. As the defect levels are Zeeman split by the externally applied magnetic field, as the field rises above the thermal energy, the upper Zeeman split energy level becomes increasingly empty. With one spin level depopulated, only the circular polarization corresponding by the lower energy spin is resonant.

We performed a pair of experiments, one with the thermal energy below the Zeeman splitting at a magnetic field of 3 T (temperature of 2.6 K), and another with a temperature comparable to the Zeeman splitting (temperature of 7 K). The results are shown in Fig. 5.4.
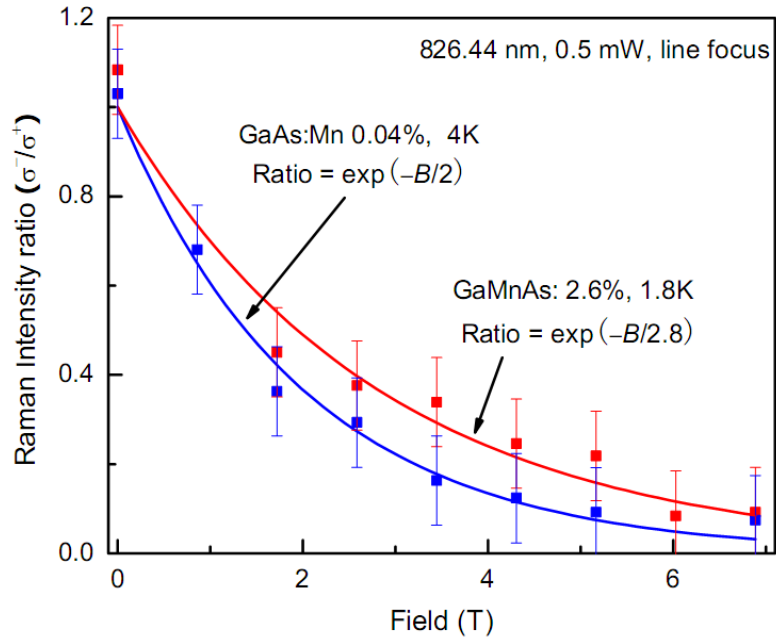
Figure 5.3 The ratio of the SIS peak intensity between orthogonal circular incident scattering polarizations as a function of magnetic field

Figure 5.4b shows a close up of the SIS data at 3 T demonstrating the difference in SIS amplitude under different incident polarizations. The SIS data is summarized in Fig. 5.4c at two different temperatures. At the higher temperature, there is no evidence of splitting up to the maximum field we could apply. At the lower temperature, the splitting is very apparent, confirming that the selection rules are related to temperature. With the earlier evidence involving the Zeeman splitting, we can conclude that the spin split level population is responsible for the selection rules observed.

Figure 5.4 a) Example of SIS data showing the transition between Mn levels at zero (bottom) and nonzero (top) magnetic f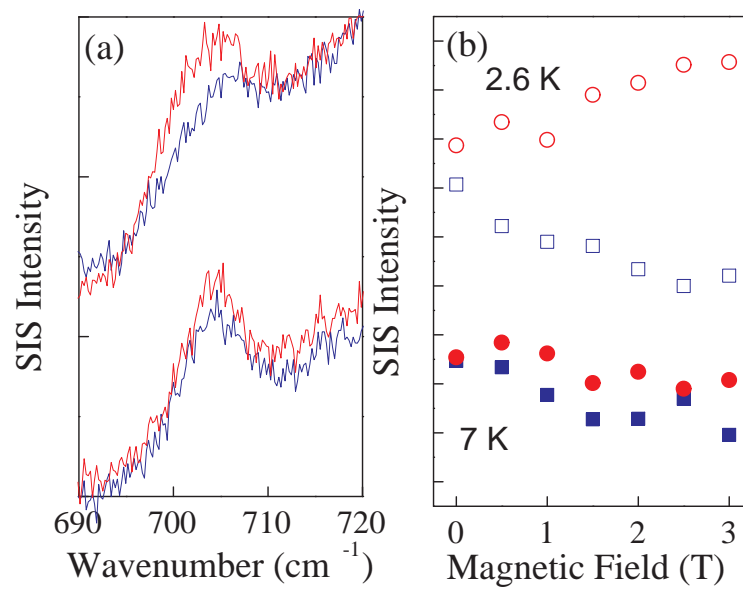ield. The two SIS curves in each case are the orthogonal circular polarizations. b) Summary of SIS data taken at different temperatures for magnetic fields up to 3 T.

Chapter 6

Conclusion

Dilute magnetic semiconductors will remain an area of intense study and research. New applications for well known magnetic systems, like the entangled electrons in the CdMnTe quantum well, continue to be developed. The properties of the material systems are still being studied, as has been done in this work for spin flip waves in CdMnTe and defects in GaMnAs. New structures, new materials, and new optical measurement techniques all provide additional means of research.

Using the system of pulse shaping and coherent control demonstrated in GaAs in chapter 2, we were able to control the spin states of isolated bound electrons in a CdMnTe quantum well, as demonstrated in chapter 3. Collective excitations in the well-understood GaAs 2DEG in a quantum well provided an ideal test of our setup. Using a pair of pulses created by the pulse shaper, the ground and excited state charge density excitations showed the expected sinusoidal dependance on pulse separation. Next, the previously established system of entangled, bound electrons in a CdMnTe quantum well was controlled in a similar fashion by a pair of pulses constructed by the pulse shaper. Taking advantage of the spatial separation of the time separated pulses from the pulse shaper, the optimal pulse pair for eliminating the single spin flip signal was constructed and shown to work as expected experimentally, leaving the double spin flip signal dominant in the spectrum. Furthermore, pump-probe measurements demonstrated the expected linear power dependence of the spin flip signals. While these simple results are promising, the coherent control measurements

demonstrate the limitations due to inhomogeneous broadening as pulse shaping with pulses separated by more than the period of the spin flip result in no measurable signal.

Advances in material quality are evident in the creation of 2DEGs in modulation doped dilute magnetic CdMnTe quantum wells. In chapter 4, we demonstrate pump-probe measurements generating spin flip waves involving the Zeeman split lowest sublevel of the quantum well and explored the mechanisms responsible for its decay. Heating dominates the spin decay even under levels of illumination considered small in other pump-probe measurements and also results in formation of zones of elevated temperature with illumination above a critical fluence. From fits to the Brillouin curve, the temperature of the magnetic system was extracted from the spin-flip wave frequency in the pump-probe measurement data. The applied external magnetic field and Mn concentration play a role in spin decay through the variation of the Mn spins and the spin polarization of the 2DEG electrons. When heating and magnetic field are carefully controlled, however, the effects of carrier excitation become evident, indicating the involvement of the heavy hole in the decay process.

The complicated GaMnAs system has been extensively studied. Grown in less than ideal conditions, GaMnAs has defect states related both to imperfections in the lattice and the Mn acting as acceptors. In this work, we have optically studied both of these in external magnetic fields. In chapter 4, data shows that the magnon modes of epitaxially grown GaMnAs depend on the material quality of grown films. Despite similar Curie temperatures, samples grown with different As species show widely varying magnon amplitudes. It is understood that As_2 grows higher quality material than As_4 during low temperature growth of GaAs. Our pump-probe measurements indicate that the interface quality also depends on the As source used. Finally, in a separate set of experiments studying paramagnetic islands in ferromagnetic GaMnAs samples, the selection rules demonstrated by transitions between Mn-related defect states were a result of the thermal population of the defect states.

Light scattering has proven very useful in studying dilute magnetic semiconductors. Optical measurements are an important tool to non-destructively measure the properties of both carrier and lattice excitations. Furthermore, these materials have shown dramatic improvement in the last two decades, and may yet prove viable for a wide variety of spintronic applications.

Appendix

Pulse Shaper Script

This is the Matlab script used to generate the desired retardances for the pulse shaper elements. The G1 and G2 refer to the two LCD arrays as shown in Fig. 1

```
clear;
%Initialize time, frequency, incoming, and target pulses
t = -10000:0.1:9999.9;
w = linspace(0.000000001, 10, 200000);
Ei = exp(j*2*t*pi*0.375).*exp(-1*(t).^2./(100)^2);


%step pulse form
%Ef = 0*t;
%Ef (99000:101000) = 1*exp(j*2*t(99000:101000)*pi*0.375);
%two pulses
Ef = exp(j*2*t*pi*0.375).*exp(-1*(t-747).^2./(100)^2)+ \\
exp(j*2*t*pi*0.375).*exp(-1*(t+747).^2./(100)^2);
%chirped pulse
%Ef = exp(j*2*t*pi*0.375).*exp(-1*(t).^2./(100)^2).* \\
exp(j*t.^2*0.0375^2*4*pi^2);
Ei = Ei ./ sum(abs(Ei));
```

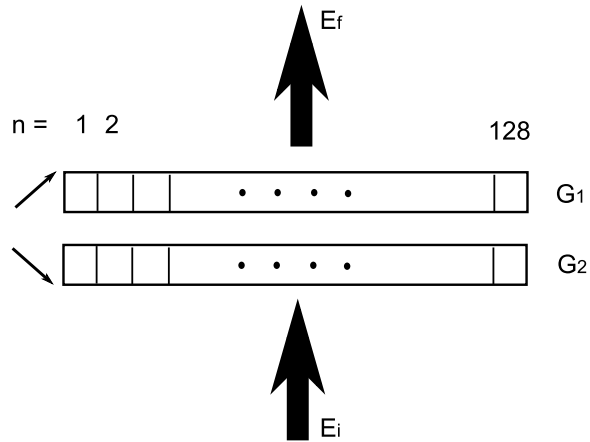**Figure 1**   Pulse Shaper.

```
Ef = Ef ./sum(abs(Ef));

Es = Ef;


%Fourier Transform of both pulses, with shifts to correct

Ewi = fft(fftshift(Ei));

Ewf = fft(fftshift(Ef));


%Calculating A coefficients and normalizing

A = Ewf./Ewi;

A = A./(max(A(7372:7629)));

A(1:7371) = 0;

A(7628:length(w)) = 0;


%Solving for retardances G1, G2

G1 = 0*t;

G2 = 0*t;

G1t = 0*t;

G2t = 0*t;
```

```matlab
for k = 7372:7627

    if (imag(A(k)) > 0.01)

        'Possible Error, imaginary part is significant';

    end

    G1t(k) = acos(real(A(k)));

    G2t(k) = -1*G1t(k);

end


%Reducing from 256 points to 128 pixels

for k = 1:128

  G1(7372+(k-1)*2)=(G1t(7372+(k-1)*2)+G1t(7373+(k-1)*2))/2;

  G1(7373+(k-1)*2)=(G1t(7372+(k-1)*2)+G1t(7373+(k-1)*2))/2;

  G2(7372+(k-1)*2)=(G2t(7372+(k-1)*2)+G2t(7373+(k-1)*2))/2;

  G2(7373+(k-1)*2)=(G2t(7372+(k-1)*2)+G2t(7373+(k-1)*2))/2;

  G1f(k) = (G1t(7372+(k-1)*2)+G1t(7373+(k-1)*2))/2;

  G2f(k) = (G2t(7372+(k-1)*2)+G2t(7373+(k-1)*2))/2;

end


q = 1:128;

G1f = G1f+2*pi;

G2f = G2f+2*pi;

file1 = fopen('output.txt', 'wt', 'n');

for k=1:128

    fprintf(file1, '%4.0f\t%4.0f\n', \\

    real(G1f(k))/pi*400-200,real(G2f(k))/pi*400+200);

end

fclose(file1);
```

Bibliography

[1] H. Akinaga, H.; Ohno. Semiconductor spintronics. *Nanotechnology, IEEE Transactions on*, 1(1):19–31, Mar 2002.

[2] J. K. Furdyna. Diluted magnetic semiconductors. *Journal of Applied Physics*, 64(4):R29–R64, 1988.

[3] J. Sadowski, J. Z. Domagała, J. Bak-Misiuk, S. Koleśnik, M. Sawicki, K. Swiatek, J. Kanski, L. Ilver, and V. Ström. Structural and magnetic properties of molecular beam epitaxy grown GaMnAs layers. volume 18, pages 1697–1700. AVS, 2000.

[4] R. Merlin. Generating coherent THz phonons with light pulses. *Sol. St. Comm.*, 102:207, 1997.

[5] S. A. Crooker, D. D. Awschalom, J. J. Baumberg, F. Flack, and N. Samarth. Optical spin resonance and transverse spin relaxation in magnetic semiconductor quantum wells. *Phys. Rev. B*, 56:7574, 1997.

[6] A. P. Heberle, J. J. Baumberg, E. Binder, T. Kuhn, K. Köhler, and K. H. Ploog. Coherent control of exciton density and spin. *IEEE J. Sel. Top. Quan. El.*, 2:769, 1996.

[7] P. Y. Yu and M. Cardona. *Fundamentals of semiconductors*. Springer-Verlag, 1996.

[8] Marc M. Wefers and Keith A. Nelson. Analysis of programmable ultrashort waveform generation using liquid-crystal spatial light modulators. *J. Opt. Soc. Am. B*, 12(7):1343, 1995.

[9] S. A. Crooker, D. D. Awschalom, and N. Samarth. Time-resolved faraday rotation spectroscopy of spin dynamics in digital magnetic heterostructures. *IEEE J. Sel. Top. Quan. El.*, 1:1082, 1995.

[10] L. Dhar, J. A. Rogers, and K. A. Nelson. Time-resolved vibrational spectroscopy in the impulsive limit. *Chem. Rev.*, 94:157, 1994.

[11] T. F. Crimmins, N. S. Stoyanov, and K. A. Nelson. Heterodyned impulsive stimulated raman scattering of phonon-polaritons in $LiTaO_3$ and $LiNbO_3$. *J. Chem. Phys.*, 117:2882, 2002.

[12] M. Trigo, T. A. Eckhause, J. K. Wahlstrand, R. Merlin M. Reason, and R. S. Goldman. Ultrafast optical generation and remote detection of terahertz sound using semiconductor superlattices. *App. Phys. Lett.*, 91:023115, 2007.

[13] J. K. Wahlstrand and R. Merlin. Cherenkov radiation emitted by ultrafast laser pulses and the generation of coherent polaritons. *Phys. Rev. B*, 68:054301, 2003.

[14] J. Zhao, A. V. Bragas, R. Merlin, and D. J. Lockwood. Magnon squeezing in antiferromagnetic MnF_2 and FeF_2. *Phys. Rev. B*, 73:184434, 2006.

[15] J. M. Bao, L. N. Pfeiffer, K. W. West, and R. Merlin. Ultrafast dynamic control of spin and charge density oscillations in a GaAs quantum well. *Phys. Rev. Lett*, 92:236601, 2004.

[16] J. M. Bao, A. V. Bragas, J. K. Furdyna, and R. Merlin. Control of sping dynamics with laser pulses: Generation of entangled states of donor-bound electrons in a $Cd_{1-x}Mn_x Te$ quantum well. *Phys. Rev. B*, 71:045314, 2005.

[17] C. Colvard, R. Merlin, M. V. Klein, and A. C. Gossard. Observation of folded acoustic phonons in a semiconductor superlattice. *Phys. Rev. Lett.*, 45:298, 1980.

[18] M. G. Cottam and D. J. Lockwood. One-magnon raman scattering in a s=5/2 antiferromagnet. *Phys. Rev. B*, 31:641, 1985.

[19] A. Pinczuk, S. Schmitt-Rink, G. Danan, J. P. Valladares, L. N. Pfeiffer, and K. W. West. Large exchange interactions in the electron gas of gaas quantum wells. *Phys. Rev. Lett.*, 63:1633, 1989.

[20] A. E. Siegman. *Lasers*. University Science Books, 1986.

[21] P. F. Moulton. Spectroscopic and laser characteristics of $Ti:Al_2O_3$. *J. Opt. Soc. Am. B*, 3:125, 1986.

[22] G. F. Albrecht, J. M. Eggleston, and J. J. Ewing. Measurements of $Ti^{3+}:Al_2O_3$ as a lasing material. *Optics Communications*, 52:401, 1985.

[23] D. R. Preuss and J. L. Gole. Three-stage birefringent filter tuning smoothly over the visible region: theoretical treatment and experimental design. *App. Optics*, 19:702, 1980.

[24] P. Bado, C. Dupuy, K. R. Wilson, R. Boggy, J. Bowen, and S. Westra. High efficiency picosecond pulse generation in the 675-930 nm region from a dye laser synchronously pumped by an argon-ion laser. *Opt. Comm.*, page 241, 1983.

[25] W. Hayes and R. Loudon. *Scattering of light by crystals*.

[26] J. Singh. *Electronic and optoelectronic properties of semiconductor structures*. Cambridge University Press, 2003.

[27] G. A. Garrett. *Femtosecond pulsed laser excitation of coherent and squeezed phonon fields (thesis)*. 2001.

[28] J. K. Wahlstrand. *Impulsive generation of coherent hybrid modes by light pulses (thesis)*. 2005.

[29] J. Bao. *Optically induced coherent intersubband excitations an spin-entangled states in semiconductor nanostructures (thesis)*. 2003.

[30] T. Stevens. *Ultrafast dynamics of low energy elementary excitations in semiconductors*. 2000.

[31] P. Horowitz and W. Hill. *The art of electronics*. Cambridge University Press, 1980.

[32] C. Chen, B. Wu, G. You, A. Jiang, and Y. Huang. High-efficiency and wide-band second-harmonic generation properties of new crystal β-Ba B_2O_4. *Dig. Tech. Papers, XIII IQEC*, page MCC5, 1984.

[33] R. Trebino, K. W. DeLong, D. N. Fittinghoff, J. N. Sweetser, M. A. Krumbügel, and B. A. Richman. Measuring ultrashort laser pulses in the time-frequency domain using frequency-resolved optical gating. *Rev. Sc. Intrum.*

[34] K. W. DeLong, D. N. Fittinghoff, and R. Trebino. Practical issues in ultrashort-laser-pulse measurement using frequency-resolved optical grating. *IEEE J. Quan. El.*, 32:1253, 1996.

[35] Ü. Özgür, C. W. Lee, and H. O. Everitt. Coherent control of coherent acoustic phonons in semiconductor quantum wells. *Phys. Rev. Lett.*, 86:5604, 2000.

[36] C. A. D. Roeser, M. Kandyla, A. Mendioroz, and E. Mazur. Optical control of coherent lattice vibrations in tellurium. *Phys. Rev. B*, 70:212302, 2004.

[37] A. M. Weiner, D. E. Leaird, G. P. Wiederrecht, and K. A. Nelson. Femtosecond multiple-pulse impulsive stimulated raman scattering spectroscopy. *J. Opt. Soc. Am. B*, 8:1264, 1991.

[38] J. K. Wahlstrand, P. Jacobs, J. M. Bao, R. Merlin, K. W. West, and L. N. Pfeiffer. Impulse excitation of cyclotron oscillations in a two-dimensional electron gas. *Sol. Stat. Comm.*, 135:574, 2005.

[39] E. Burstein, G. S. Picus, and H. A. Gebbie. Cyclotron resonance at infrared frequencies in InSb at room temperature. *Phys. Rev.*, 103:825, 1956.

[40] R. Borroff, R. Merlin, J. Pamulapati, P. K. Bhattacharya, and C. Tejedor. Raman scattering by coupled intersubband-landau-level excitations in quantum-well structures. *Phys. Rev. B*, 43:2081, 1991.

[41] S. Das Sarma and D. Wang. Resonant raman scattering by elementary electronic excitations in semiconductor structures. *Phys Rev. Lett.*, 83:816, 1999.

[42] S. Katayama and T. Ando. Light scattering by electronic excitations in n-type GaAs-Al$_x$Ga$_{1-x}$As superlattices. *J. Phys. Soc. Japan*, 54:1615, 1985.

[43] G. Brozak, B. V. Shanabrook, D. Gammon, and D. S. Katzer. Collective intersubband spin- and charge-density excitations in tilted magnetic fields. *Phys. Rev. B*, 47:9981, 1993.

[44] H. Barkhuijsen, R. de Beer, W. M. M. J. Bovee, and D. van Ormondt. Retrieval of frequencies, amplitudes, damping factors, and phases from time-domain signals using a linear least-squares procedure. *J. Mag. Res.*, 61(3):465–481, 1985.

[45] Xinhua Peng, Jiangfeng Du, and Dieter Suter. Quantum phase transition of ground-state entanglement in a heisenberg spin chain simulated in an NMR quantum computer. *Physical Review A (Atomic, Molecular, and Optical Physics)*, 71(1):012307, 2005.

[46] Michael A. Nielsen and Isaac L. Chuang. *Quantum Computation and Quantum Information*. Cambridge University Press, 2000.

[47] D. P. DiVincenzo. The physical implementation of quantum computation. *Fortschritte der Physik*, 48(9-11):771–783, 2000.

[48] P. C. Haljan, P. J. Lee, K-A. Brickman, M. Acton, L. Deslauriers, and C. Monroe. Entanglement of trapped-ion clock states. *Physical Review A (Atomic, Molecular, and Optical Physics)*, 72(6):062316, 2005.

[49] J. A. Jones and M. Mosca. Implementation of a quantum algorithm on a nuclear magnetic resonance quantum computer. *The Journal of Chemical Physics*, 109(5):1648–1653, 1998.

[50] Yuriy Makhlin, Gerd Schön, and Alexander Shnirman. Quantum-state engineering with Josephson-junction devices. *Rev. Mod. Phys.*, 73(2):357–400, May 2001.

[51] Guido Burkard. Spin-entangled electrons in solid-state systems. *Journal of Physics: Condensed Matter*, 19(23):233202 (24pp), 2007.

[52] E. Merzbacher. *Quantum Mechanics*. John Wiley & Sons, Inc., 1998.

[53] J. Bao, A. V. Bragas, J. K. Furdyna, and R. Merlin. Optically induced multispin entanglement in a semiconductor quantum well. *Nat. Mat.*, 2:175, 2003.

[54] F. Bassani, S. Tatarenko, K. Saminadayar, N. Magnea, R. T. Cox, A. Tardot, and C. Grattepain. Indium doping of CdTe and Cd$_{1-x}$Zn$_x$Te by molecular-beam epitaxy: Uniformly and planar-doped layers, quantum wells, and superlattices. *J. Appl. Phys.*, 72:2927, 1992.

[55] J. A. Gaj, R. Planel, and G. Fishman. Relation of magneto-optical properties of free excitons to spin alignment of Mn^{2+} ions in Cd$_{1-x}$Mn$_x$Te. *Sol. St. Com.*, 29:435, 1979.

[56] R. W. Martin, R. J. Nicholas, G. J. Rees, S. K. Haywood, N. J. Mason, and P. J. Walker. Two-dimensional spin confinement in strained-layer quantum wells. *Phys. Rev. B*, 42:9237, 1990.

[57] P. Peyla, A. Wasiela, and Y. M. d'Aubigné. Anisotropy of the Zeeman effect in CdTe/Cd$_{1-x}$Mn$_{Te}$ multiple quantum wells. *Phys. Rev. B*, 47:3783, 1993.

[58] B. Kuhn-Heinrich, W. Ossau, E. Bangert, A. Waag, and G. Landwehr. Zeeman pattern of semimagnetic (CdMn)Te/(CdMg)Te quantum wells in inplane magnetic fields. *Sol. St. Com.*, 91:413, 1994.

[59] B. Kuhn-Heinrich and W. Ossau. Anisotropy of excitonic zeeman splitting and the relation to exchange effects in semimagnetic heterostructures. *Mat. Sci. For.*, 182-184:491, 1995.

[60] J. Stühler, G. Schaack, M. Dahl, A. Waag, G. Landwehr, K. V. Kavokin, and I. A. Merkulov. Multiple mn^{2+}-spin-flip raman scattering at high fields via magnetic polaron states in semimagnetic quantum wells. *Phys. Rev. Lett.*, 74(13):2567–2570, Mar 1995.

[61] D. L. Peterson, D. U. Bartholomew, U. Debska, A. K. Ramdas, and S. Rodriguez. Spin-flip raman scattering in n-type diluted magnetic semiconductors. *Phys. Rev. B*, 32:323, 1985.

[62] D. Heiman, P. A. Wolff, and J. Warnock. Spin-flip raman scattering, bound magnetic polaron, and fluctuations in (Cd,Mn)Se. *Phys. Rev. B*, 27:4848, 1983.

[63] J. Stühler, G. Schaack, M. Dahl, A. Waag, G. Landwehr, K. V. Kavokin, and I. A Merkulov. Multiple Mn^{2+}-spin flip Raman scattering at high fields via magnetic polaron states in semimagnetic quantum wells. *Phys. Rev. Lett.*, 74:2567, 1995.

[64] A. Petrou, D. L. Peterson, S. Venugopalan, R. R. Galazka, A. K. Ramdas, and S. Rodriguez. Raman scattering study of the magnetic excitations in diluted magnetic semiconductors in the presence of an external magnetic field. *Phys. Rev. B*, 27:3471, 1983.

[65] G. Karczewski, J. Jaroszyski, A. Barcz, M. Kutrowski, T. Wojtowicz, and J. Kossut. High mobility 2D electron gas in iodine modulation doped CdTe/CdMgTe heterostructures. *J. Crys. Growth*, 184-185:814–817, 1998.

[66] V. E. Kirpichev, L. V. Kulik, I. V. Kukushkin, K. v. Klitzing, K. Eberl, and W. Wegscheider. Direct observation of the intersubband bernstein modes: Many-body coupling with spin- and charge-density excitations. *Phys. Rev. B*, 59:R12 751, 1999.

[67] F. Perez, C. Aku-leh, D. Richards, B. Jusserand, L.C. Smith, D. Wolverson, and G. Karczewski. From spin flip excitations to the spin susceptibility enhancement of a two-dimensional electron gas. *Phys. Rev. Lett.*, 99:026403, 2007.

[68] D. Gammon, B. V. Shanabrook, J. C. Ryan, and D. S. Katzer. Spin-density waves in a quasi-two-dimensional electron gas. *Phys. Rev. B*, 41:12311, 1990.

[69] O. Gunnarsson and B. I. Lundqvist. Exchange and correlation in atoms, molecules and solids by the spin-density-functional formalism. *Phys. Rev. B*, 13:4274, 1976.

[70] B. Jusserand, F. Perez, D. R. Richards, G. Karczewski, T. Wojtowicz, C. Testelin, D. Wolverson, and J. J. Davies. Spin excitations of the spin-polarized electron gas in semimagnetic quantum wells. *Phys. Rev. B*, 91:086802, 2003.

[71] R. J. Elliott. Theory of the effect of spin-orbit coupling on magnetic resonance in some semiconductors. *Phys. Rev.*, 96:266, 1954.

[72] P. H. Song and K. W. Kim. Spin relaxation of conduction electrons in bulk III-V semiconductors. *Phys. Rev. B*, 66:035207, 2002.

[73] M. I. D'yakonov and V. I. Perel. Spin relaxation of conduction electrons in noncentrosymmetric semiconductors. *Sov. phys. Sol. St.*, 13:3023, 1972.

[74] F. X. Bronold, I. Martin, A. Saxena, and D. Smith. Magnetic-field dependence of electron spin relaxation in n-type semiconductors. *Phys. Rev. B*, 66:233206, 2002.

[75] G. L. Bir, A. G. Aronov, and G. E. Pikus. Spin relaxation of electrons due to scattering by holes. *Sov. Phys.-JETP*, 42:705, 1975.

[76] K. E. Roennburg, E. Mohler, H. G. Roskos, K. Ortner, C. R. Becker, and L. W. Molenkamp. Motional-narrowing-type dephasing of electron and hole spins of itinerant excitons in magnetically doped II-VI bulk semiconductors. *Phys. Rev. Lett.*, 96:117203, 2006.

[77] G. Bastard and L. L. Chang. Spin-flip relaxation time of conduction electrons in $Cd_{1-x}Mn_xTe$ quantum wells. *Phys. Rev. B*, 41:7899, 1990.

[78] C. Camilleri, F. Teppe, D. Scalbert, Y. G. Semenov, M. Nawrocki, M. Dyakonov, J. Cibert, S. Tatarenko, and T. Wojtowicz. Electron and hole spin relaxation in modulation-doped CdMnTe quantum wells. *Phys. Rev. B*, 64:085331, 2001.

[79] C. Aku-Leh, F. Perez, B. Jusserand, D. Richards, W. Pacuski, P. Kossacki, M. Menant, and G. Karczewski. Measuring the spin polarization and zeeman energy of a spin-polarized electron gas: comparison between raman scattering and photoluminescence. *Phys. Rev. B*, 76:155416, 2007.

[80] F. Fischer, A. Waag, G. Bilger, Th. Litz, S. Scholl, M. Schmitt, and G. Landwehr. Molecular beam epitaxy of iodine-doped CdTe and (CdMg)Te. *J. Crys. Growth*, 141:93–97, 1994.

[81] T. Ando, A. B. Fowler, and F. Stern. Electronic properties of two-dimensional systems. *Rev. Mod. Phys.*, 54:437, 1982.

[82] B. E. Larson, K. C. Hass, H. Ehrenreich, and A. E. Carlsson. Theory of exchange interactions and chemical trends in diluted magnetic semiconductors. *Phys. Rev. B*, 37:4137, 1988.

[83] F. Perez, B. Jusserand, D. Richards, and G. Karczewski. Spin waves of the spin-polarized electron gas in semimagnetic quantum wells. *Phys. Stat. Sol. b*, 243:873, 2006.

[84] F. Teppe, M. Vladimirova, D. Scalbert, T. Wojtowicz, and J. Kossut. Optically induced instability of spin precession in magnetic quantum wells. *Phys. Rev. B*, 67:033304, 2003.

[85] M. Vladimirova, D. Scalbert, and C. Misbah. Pattern formation in paramagnetic diluted magnetic semiconductors. *Phys. Rev. B*, 71:233203, 2005.

[86] H. Ohno. Molecular beam epitaxy and properties of ferromagnetic III-V semiconductors. *J. Crys. Grow.*, 251:285, 2003.

[87] T. Jungwirth, Jairo Sinova, J. Masek, J. Kucera, and A. H. MacDonald. Theory of ferromagnetic (III,Mn)V semiconductors. *Reviews of Modern Physics*, 78(3):809, 2006.

[88] D. C. Look, D. C. Walters, M. O. Manasreh, J. R. Sizelove, C. E. Stutz, and K. R. Evans. Anomalous hall-effect results in low-temperature molecular-beam-epitaxial GaAs: Hopping in a dense EL2-like band. *Phys. Rev. B*, 42:3578, 1990.

[89] T. Dietl, H. Ohno, and F. Matsukara. Hole-mediated ferromagnetism in tetrahedrally coordinated semiconductors. *Phys. Rev. B*, 63:195205, 2001.

[90] C. Zener. Interaction between the d shells in the transition metals. *Phys. Rev.*, 81:440, 1951.

[91] C. Kittel M. A. Ruderman. Indirect exchange coupling of nuclear magnetic moments by conduction band electrons. *Phys. Rev.*, 96:99, 1954.

[92] M. Linnarsson, E. Janzén, B. Monemar, M. Kleverman, and A. Thilderkvist. Electronic structure of the gaas:Mn$_{Ga}$ center. 55:6938, 1997.

[93] V. F. Sapega, M. Moreno, M. Ramsteiner, L. Dẅeritz, and K. H. Ploog. Polarization of valence band holes in the (Ga,Mn)As diluted magnetic semiconductor. 94:137401, 2005.

[94] D. Wang. *Optical studies of spin dynamics and hole transitions in ferromagnetic semiconductor (Ga,Mn)As*. 2007.

[95] D. M. Wang, Y. H. Ren, X. Liu, J. K. Furdyna, M. Grimsditch, and R. Merlin. Light-induced magnetic precession in (Ga,Mn)As slabs: Hybrid standing-wave damoneshbach modes. *Phys. Rev. B*, 75:233308, 2007.

[96] R. W. Damon and J. R. Eshbach. Magnetostatic modes of a ferromagnet slab. *J. Phys. Chem. Sol.*, 19:308, 1961.

[97] M. van Kampen, C. Jozsa, J. T. Kohlhepp, P. LeClair, L. Lagae, W. J. M. de Jonge, and B. Koopmans. All-optical probe of coherent spin waves.

[98] B. S. Krusor and R. Z. Bachrach. Two-stage arsenic cracking source with integral getter pump for MBE growth. *J. Vac. Sci. Tech. B*, 1:138, 1983.

[99] R. P. Campion, K. W. Edmonds, L. X. Zhao, K. Y. Wang, C. T. Foxon, B. L. Gallagher, and C. R. Staddon. High-quality gamnas films grown with arsenic dimers. *J. Crys. Grow.*, 247:42, 2003.